1 **Marine anoxia initiates giant sulfur-bacteria mat proliferation and associated changes in**

2 **benthic nitrogen, sulfur, and iron cycling in the Santa Barbara Basin, California**

3 **Borderland**

4 David J. Yousavich[1*], De'Marcus Robinson[2], Xuefeng Peng[3], Sebastian J. E. Krause[1,4], Frank

5 Wenzhöfer[5,6,7], Felix Janssen[5,6], Na Liu[8], Jonathan Tarn[8], Frank Kinnaman[8], David L. Valentine[8],

6 Tina Treude[1,2*]

7

8 [1]Department of Earth, Planetary, and Space Sciences, University of California Los Angeles, 595 Charles E.

9 Young Drive East, Los Angeles, CA 90095, USA

10 [2]Department of Atmospheric and Oceanic Sciences, University of California Los Angeles, Math Science

11 Building, 520 Portola Plaza, Los Angeles, CA 90095, USA

12 [3]School of Earth, Ocean, and Environment, University of South Carolina, 701 Sumter Street, EWS 617,

13 Columbia, SC 29208, USA

14 [4]Earth Research Institute, 6832 Ellison Hall, University of California Santa Barbara, Ca 93106-3060

15 [5]HGF-MPG Joint Research Group for Deep-Sea Ecology and Technology, Alfred-Wegener-Institute,

16 Helmholtz-Center for Polar and Marine Research, Am Handelshafen 12, 27570 Bremerhaven, Germany

17 [6] HGF-MPG Joint Research Group for Deep-Sea Ecology and Technology, Max Planck Institute for Marine

18 Microbiology, Celsiusstrasse 1, 28359 Bremen, Germany

19 [7]Department of Biology, DIAS, Nordcee and HADAL Centres, University of Southern Denmark, 5230 Odense

20 M, Denmark

21 [8]Department of Earth Science and Marine Science Institute, University of California, Santa Barbara, CA

22 93106, USA

23

24 **Correspondence:** David Yousavich (yousavdj@ucla.edu), Tina Treude (ttreude@g.ucla.edu)

Abstract

The Santa Barbara Basin naturally experiences transient deoxygenation due to its unique geological setting in the Southern California Borderland and seasonal changes in ocean currents. Long-term measurements of the basin showed that anoxic events and subsequent nitrate exhaustion in the bottom waters have been occurring more frequently and lasting longer over the past decade. One characteristic of the Santa Barbara Basin is the seasonal development of extensive mats of benthic nitrate-reducing sulfur-oxidizing bacteria, which are found at the sediment-water interface when the basin's bottom waters reach anoxia but still provide some nitrate. To assess the mat's impact on the benthic and pelagic redox environment, we collected biogeochemical sediment and benthic flux data in November 2019, after anoxia developed in the deepest waters of the basin and dissolved nitrate was depleted (down to 9.9 µM). We found that the development of mats was associated with a shift from denitrification to dissimilatory nitrate reduction to ammonium. The zone of sulfate reduction appeared near the sediment-water interface in sediment hosting these ephemeral white mats. We found that an exhaustion of iron oxides in the surface sediment was an additional prerequisite for mat proliferation. Our research further suggests that cycles of deoxygenation and reoxygenation of the benthic environment result in extremely high benthic fluxes of dissolved iron from the basin's sediment. This work expands our understanding of nitrate-reducing sulfur-oxidizing mats and their role in sustaining and potentially expanding marine anoxia.

Introduction

Naturally occurring low-oxygen waters in the ocean are commonly observed below the ocean's mixed layer where respiration consumes oxygen faster than it is produced or ventilated. When low oxygen conditions occur along the western continental shelf in regions susceptible to upwelling events and/or undergoing eutrophication, organic matter remineralization can frequently drive oxygen concentrations to hypoxic ($O_2 < 63$ μM) (Middelburg and Levin, 2009) and/or anoxic levels ($O_2 < 3$ μM) (Fossing et al., 1995b; Canfield et al., 2010). These areas are usually referred to as Oxygen Minimum Zones (OMZs). In the water column of OMZs, nitrogen reduction becomes an important mechanism for organic matter remineralization (Ward et al., 2009). OMZs within coastal basins that experience seasonal changes in upwelling can experience anoxic and nitrate reducing conditions that extend to the benthic environment, especially when high productivity and associated organic matter export coincide with seasonal patterns of physical mixing. This fundamental change in the redox conditions at the sediment-water interface encourages elevated rates of anaerobic microbial processes and can promote organic matter preservation in the sediments (Middelburg and Levin, 2009; Treude, 2011), though a recent study suggests a thin reactive surface layer can provide high rates of organic matter degradation in anoxic environments (Van De Velde et al., 2023). Persistent anoxia in these coastal OMZ can lead to huge releases of sulfide (up to 13.7 mmol m^{-2} d^{-1}) and ammonium (up to 21.2 mmol m^{-2} d^{-1}) into the water column (Sommer et al., 2016).

The Santa Barbara Basin (SBB) is an example of one of these coastal OMZs that experiences seasonal deoxygenation. Drastic changes in water column oxygenation and seafloor redox

68   conditions drive complex changes in benthic biogeochemistry and microbiology, evidenced most

69   clearly by the development of thick, expansive mats of giant sulfur-oxidizing bacteria (GSOB)

70   on the SBB seafloor (Bernhard et al., 2003; Prokopenko et al., 2006; Valentine et al., 2016;

71   Kuwabara et al., 1999). A 2016 survey of the basin identified a vast GSOB mat spread over 1.6

72   contiguous km, confined between 487 and 523 km in the SBB depocenter where conditions were

73   anoxic but not depleted of NO_3^- (Valentine et al., 2016). These GSOB mats have been noted

74   previously in the SBB benthos, appearing at times of anoxia and disappearing when oxygen is

75   present in the bottom water (Reimers et al., 1996b; Kuwabara et al., 1999). Similar GSOB mats

76   have been identified in other transiently deoxygenated OMZs such as the Peruvian/Chilean coast

77   (Sommer et al., 2016; Schulz et al., 1996; Zopfi et al., 2001; Høgslund et al., 2009). The

78   chemoautotrophic bacteria that constitute the bulk of GSOB mats (typically *Thioploca* and/or

79   *Beggiatoa*) utilize sulfide as an electron donor and O_2 or NO_3^- as a terminal electron acceptor

80   (Jørgensen and Nelson, 2004). Some GSOB can hyperaccumulate NO_3^- in cell vacuoles up to

81   500 mM (Fossing et al., 1995a) and use this NO_3^- reserve to oxidize sulfide that diffuses from the

82   underlying sediment to perform their metabolism. (Huettel et al., 1996; Mußmann et al., 2003;

83   Sayama, 2001).
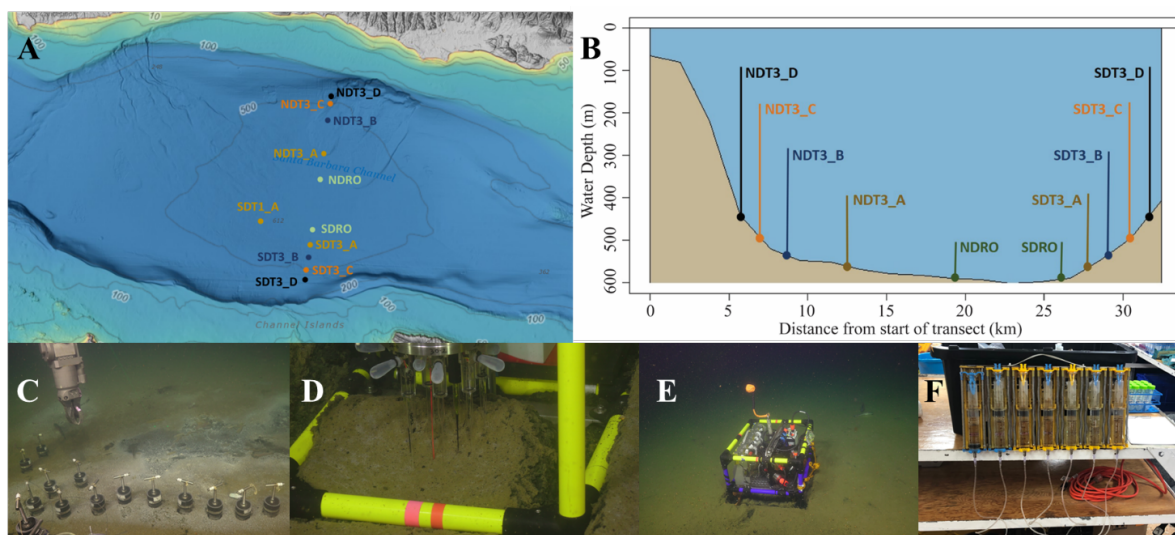
84

85
86 **Figure 1. Maps of sampling locations in the Santa Barbara Basin and photographs of**
87 **deployed equipment:** (A) bathymetric map of the Santa Barbara Basin with locations of all
88 sampled stations; (B) cross-section of the Santa Barbara Basin with locations of all sampled
89 station; (C) sediment push coring with ROV arm; (D) sediment microprofiler; (E) benthic flux
90 chamber; (F) closeup of a syringe system from a benthic flux chamber. The map in (A) was
91 generated using the Bathymetric Data Viewer provided by the National Centers for
92 Environmental Information.
93

94 The activity of GSOB mats contribute significantly to element cycling in benthic marine

95 environments with large effects on biogeochemical conditions in the bottom water. Isotopic

96 measurements of $^{15}N/^{14}N$ and $^{18}O/^{16}O$ from NO_3^- in the SBB water column suggest that benthic

97 organisms are responsible for approximately 75% of the total NO_3^- reduction in the SBB

98 (Sigman et al., 2003). Other studies found that GSOB mats inhibit the diffusion of NO_3^- into

99 sediments via hyper-accumulation in vacuoles thereby creating conditions ideal for bacterial

100 heterotrophic sulfate reduction beneath them (Fossing et al., 1995b; Zopfi et al., 2001). These

101 studies suggest that GSOB mats in the SBB may be responsible for the majority of NO_3^-

102 consumption in the basin rather than water-column microbes. Additionally, GSOB mats have

103 been reported to deplete NO_3^- via dissimilatory nitrate reduction to ammonia (DNRA) in the

104 anoxic bottom water of the Peruvian OMZ (Dale et al., 2016) and in the hypoxic transition zone

105 in the Eastern Gotland Basin of the Baltic Sea (Noffke et al., 2016). By contrast, benthic

106 microbial communities in the hypoxic (42 μM) Mauritanian OMZ perform canonical

107 denitrification instead (Dale et al., 2014). The contrast between the Peruvian and Mauritanian

108 OMZ suggests that bottom- water anoxia triggers the appearance of GSOB mats, and that DNRA

109 is more prevalent where GSOB mats are present.

110

111   The rapid accumulation and consumption of NO_3^- by GSOB mats has ramifications for the redox

112   conditions in the sediment underneath. The depletion of NO_3^- and shallowing of the nitracline

113   could promote high rates of sulfate reduction in the sediment underneath the GSOB mat. In

114   return, the sulfate reduction zone exists close to the sediment-water interface, providing the

115   GSOB mat with readily accessible sulfide. If a metabolic feedback loop is then established

116   between sulfur-oxidizing bacteria at the sediment-water interface and sulfate-reducing bacteria in

117   the sediment, increased NO_3^- loss from the water column and spreading of sulfidic conditions in

118   SBB sediment is expected. With these mats being potentially crucial to nitrogen and sulfur

119   cycling in sediments underlying OMZs, their biogeochemical transformations and ergo effect

120   upon basin redox conditions are critically important to understanding element cycling in the

121   SBB. Such gained knowledge would have additional benefits for predicting biogeochemical

122   feedbacks to the projected expansion of oceanic oxygen deficiency, in the SBB and in OMZs

123   more general, as a result of global change (Stramma et al., 2008).

124

125   Utilizing in-situ technologies, sediment porewater extraction, solid phase analyses, and

126   radiotracer techniques, this study aims to answer the following overarching questions: (1) Which

127   environmental conditions initiate and sustain the proliferation of GSOB mats? (2) Which

128   biogeochemical transformations occur in the sediment underneath these mats? (3) What role do

129   the mats play in the increasingly prevalent anoxic and nitrate-depleted condition found in the

130   SBB? These investigations represent the first basin-wide geochemical characterization of the

131   Santa Barbara Basin which hosts the largest as-of-yet mapped GSOB mat in the world's oceans.

132   It is the first suite of in-situ flux measurements carried out in the SBB, which is unique to other

133   heavily studied marine settings (e.g., Eastern Gotland Basin, Peruvian upwelling zone) in that it

134   is an oceanic basin within an upwelling zone. The results presented here also provide

135   geochemical context for a number of other related investigations in the SBB (Robinson et al.,

136   2022; Peng et al., 2023) as well as the first measurements in a multi-year study of

137   biogeochemical changes in response to warming waters and increased stratification on the

138   California coast.

2. Materials and Methods

2.1 Study Site

The Santa Barbara Basin (SBB) is a coastal basin in the California Borderland with an approximate maximum depth of 600 m characterized by a seasonally anoxic water column (Sverdrup and Allen, 1939; Sholkovitz and Gieskes, 1971). The transform boundary along the California Borderland heavily affects the geomorphology of basins in this region; these basins become twisted as the plates rub against each other and form a series of "bathtubs" blocked by sills and seamounts off the coast of California. The SBB is bordered by the California coast in the north, the Channel Islands in the south, the Santa Monica basin to the east, and the Arguello Canyon to the west. A sill to the west of the basin at around 475 m depth (Fig. 1) prohibits most water transfer between the Santa Lucia Slope and the deeper waters of the SBB (Sholkovitz and Gieskes, 1971). The highly productive surface waters in the basin provide ample organic matter to the basin's water column, encouraging strong remineralization processes below the euphotic zone, which can induce anoxia below the sill depth, with typically less than 1 µmol O_2 L^{-1} (Sholkovitz, 1973; Emery et al., 1962; Thunell, 1998; Emmer and Thunell, 2000). Benthic faunal distribution within the basin is tightly correlated with this sill depth and related oxygen conditions; below the sill, the sea snail *Alia permodesta* is the most commonly found benthic fauna, while sea stars, sea urchins, and other echinoderms increase in density above the sill (Myhre et al., 2018). During upwelling events (usually in Spring), oxygenated waters from the California Current spill over the western sill and ventilate the SBB, reportedly increase bottom water oxygen concentrations to approximately 20 µmol O_2 L^{-1} (Goericke et al., 2015). SBB water-column oxygen and nitrogen concentrations have been evaluated through a longitudinal survey by the California Cooperative Oceanic Fisheries Investigations (Calcofi) with data

162   starting in the 1950's . The data collected by this survey shows increasing durations of anoxia

163   and fixed nitrogen loss in the basin with the SBB becoming completely nitrate-depleted below

164   the sill at least three times between 2012 and 2017 (https://calcof.iorg/data/).

165

166   **2.2 Benthic sediment sampling and instrument deployment**

167   Sediment samples were taken between 30 October and 11 November 2019 during an expedition

168   aboard the research vessel *(R/V) Atlantis* equipped with the remote operated vehicle (ROV)

169   Jason. Samples were taken at stations along a bimodal, north-south transect through the

170   depocenter of the SBB, as well as one station on a separate transect. Details of sampling stations

171   can be seen in Fig. 1A and 1B. Briefly, depocenter stations are labeled as NDRO and SDRO

172   (northern and southern depocenter radial origin, respectively). The remaining stations are named

173   for the cardinal direction (north vs. south) and the transect number (e.g., SDT1-A is on transect 1

174   while SDT3-A is on transect 3). As station depth decreases, the alpha suffix increases (e.g.,

175   NDT3-A is deeper than NDT3-B, etc.).

176

177   ROV Jason conducted sediment push coring and deployed automated benthic flux chambers

178   (BFC) and microprofilers at each station. Bottom water oxygen concentration was determined

179   using an Aanderaa 4831 oxygen optode (Aanderaa Instruments, Bergen, Norway) installed on

180   the ROV. Optical modems (Luma 250LP, Hydromea, Renens, Switzerland) installed on the ROV

181   and the BFC and microprofilers were used to transmit deployment settings and start/terminate

182   measurements of the instruments. Multiple push cores (polycarbonate, 30.5 cm length, 6.35 cm

183   inner diameter) per sampling station were retrieved during ROV Jason deployments (Fig. 1C).

184   Replicate cores from each station were transferred to an onboard 6°C cold room upon recovery

185 aboard the ship and subsampled for either solid phase analyses, porewater geochemistry, or

186 radiotracer experiments.

187

188 **2.3 Sediment Core Sub-Sampling**

189 Two replicate ROV push cores that were collected near each other at each station were processed

190 under a constant argon flow to protect redox-sensitive species. Cores were sectioned in 1-cm

191 increments up to 10 cm followed by 2-cm increments. Note, sediments from the NDT3-B station

192 were sliced in 2-cm increments. Sediment subsections were transferred into argon-filled 50-mL

193 conical centrifuge tubes. Sediment samples were centrifuged at 2300 x g for 20 minutes. The

194 centrifugate was subsampled unfiltered as fast as possible (to avoid contaminations with oxygen)

195 for porewater analyses. Solid phase cores were sectioned similar to porewater cores and sub-

196 sampled for sediment density, porosity, and organic matter content. A 10 mL cut-off plastic

197 syringe was used to collect 6 mL of sediment into pre-weighed plastic vials (15 mL snap-cap

198 vials) and stored in the dark at 4°C for sediment porosity and density analysis. Two-mL

199 microcentrifuge tubes were filled with sediment from each depth interval and stored at -30°C for

200 sediment organic matter analyses. One ROV push core per station was sub-sampled with a

201 miniaturized push core (length 20 cm, inner diameter 2.6 cm) and taken immediately to the

202 shipboard radioisotope van for radiotracer experiments (see section 2.5).

203

204 **2.4 Sediment Porewater Geochemistry**

205 Concentrations of porewater sulfide (Cline, 1969), NH_4^+, PO_4^{3-}, and Fe^{2+} (Grasshoff et al., 1999)

206 were determined shipboard with a Shimadzu UV-Spectrophotometer (UV-1800). Detection

207 limits for sulfide, NH_4^+, PO_4^{3-}, and Fe^{2+} were 1 μM. Subsamples (2 mL) for porewater NO_3^- and

208   NO_2^- concentrations were stored in 2-mL plastic vials with an O-ring, frozen shipboard at -30°C

209   and analyzed back at the home laboratory on the same spectrophotometer using the method

210   following (García-Robledo et al., 2014). The detection limit for NO_3^- and NO_2^- was 0.5 µM.

211   Samples for porewater DIC were preserved shipboard with 5 µL saturated HgCl in headspace

212   free glass vials and stored at 4°C for later analysis following (Hall and Aller, 1992). DIC

213   detection limit was 0.1 mM. Total alkalinity was determined shipboard using direct titration of

214   500 µL of pore water with 0.01M Titrisol® HCl (Pavlova et al., 2008). The analysis was

215   calibrated using IAPSO seawater standard, with a precision and detection limit of 0.05 meq L^{-1}.

216   Subsamples (1 mL) for sulfate and chlorinity were stored in 2-mL plastic vials with an O-ring,

217   frozen shipboard at -30°C and later measured in the lab using a Metrohm 761 ion chromatograph

218   with a methodological detection limit of 30 µM (Dale et al., 2015).

219

220   **2.5 Solid Phase Analyses**

221   Porosity/Density samples were collected in pre-weighed plastic vials and dried at 50°C for up to

222   96 hr until the dry weight was stable. Sediment porosity was calculated by taking the difference

223   between wet and dry sediment weight and divided by the volume of the wet sediment. Sediment

224   density was calculated by dividing the wet sediment weight by its volume. Treatment of

225   sediment subsamples for total organic carbon (TOC), total organic nitrogen (TON), and organic

226   carbon isotope composition ($\delta^{13}C$) were modified from (Harris et al., 2001) and sent to the

227   University of California Davis Stable Isotope Facility for analysis using Elemental Analyzer –

228   Isotope Ratio Mass Spectrometry. TOC and TON were calculated based on the sample peak area

229   corrected against a reference material (alfalfa flour). Limit of quantification based on peak area

230   was 100 µg C with an uncertainty of ± 0.2 ‰ for $\delta^{13}C$.

231

2.6 Sulfate Reduction

To determine ex-situ microbial sulfate reduction rates, whole round sub-cores were injected with 10 µL carrier-free ^{35}S-Sulfate radiotracer (dissolved in water, 200 kBq, specific activity 37 TBq $mmol^{-1}$) into pre-drilled, silicon-filled holes at 1-cm increments according to (Jørgensen, 1978). These sub-cores were incubated at 6°C in the dark for 6-8 hours. Incubations were stopped by slicing sediment cores in 1-cm increments into 50-mL centrifuge tubes filled with 20-mL zinc acetate (20% w/w) and frozen at -20°C until analysis at the land-based laboratory. Microbial activity in controls was terminated with zinc acetate (20 mL of 20% w/w) before the addition of radiotracer and subsequent freezing. Lab-based analysis of sulfate reduction rates were determined following the cold-chromium distillation procedure (Kallmeyer et al., 2004).

242

2.7 Benthic In-Situ Investigations

Per station, one to three microprofiler (Fig. 1D) and three BFC (Fig. 1E) deployments were carried out by the ROV Jason at the seafloor. Construction, deployment and operation of automated microprofilers and BFCs followed those described in (Treude et al., 2009). The microprofiler deployed in this study represents a modified, miniaturized version of the instrument described in (Gundersen and Jørgensen, 1990) that was constructed specifically for use by ROV. Microprofilers were outfitted with three O_2-microelectrodes (Glud et al., 2000), two pH-microelectrodes (Revsbech and Jørgensen, 1986), two H_2S-microelectrodes (Jeroschewsky et al., 1996), and one conductivity sensor to determine the position of the sediment-water interface relative to the tips of the microelectrodes. Concentrations of oxygen

253   and sulfide, as well as pH were each calculated from microelectrode readings and averaged for

254   the respective sites where replicates existed.

255

256   The BFC consisted of a frame equipped with a cylindrical polycarbonate chamber (inner

257   diameter = 19 cm) with its lower portion sticking out of the frame. The upper side of the

258   chamber was closed by a lid containing a stirrer (Type K/MT 11, K.U.M., Kiel, Germany),

259   oxygen optodes (Type 4330, Aanderaa Data Instruments, Bergen Norway and Hydroflash,

260   Contros/Kongsberg Maritime, Kongsberg, Norway), a conductivity sensor (type 5860, Aanderaa

261   Data Instruments), and a valve. Prior to insertion into the sediments, the chambers were held

262   upside down by the ROV manipulating arms within approximately 10 m of the seafloor and

263   moved back and forth to make sure that water from shallower depth that may have been trapped

264   was replaced by bottom water. Chamber incubations lasted between 240 and 390 minutes. Each

265   BFC was outfitted with a custom-built syringe sampler containing seven syringes that were

266   connected by tubes to sampling ports in the upper wall of the chambers (Fig. 1F): one injection

267   syringe and six sampling syringes that were fired at regular time intervals over the time course of

268   the deployment. The injection syringe contained de-ionized water and the reduction in salinity in

269   the overlaying water after salinity readings stabilized (i.e., full mixing was achieved) 10-30 min

270   after injection was used to determine BFC volumes (Kononets et al., 2021). Samples obtained

271   from the overlaying water of the BFC were examined for the same geochemical constituents as

272   described above (section 2.4). Benthic fluxes of NO_3^-, NH_4^+, PO_4^{3-}, and Fe^{2+} were calculated as

273   follows:

274

275     $J = \frac{\Delta c}{\Delta t} * \frac{V}{A}$ (EQ # 2)

276

277   Where J is the flux in mmol m^{-2} d^{-1}, ΔC is the concentration change in mmol m^{-3}, Δt is the time

278   interval in d, V is the overlying water volume in m^3, and A is the surface area of the sediment

279   covered by the benthic flux chamber in m^2. An average flux within BFC's was calculated for

280   stations of similar depth. One chamber per site contained $^{15}N-NO_3^-$ in the injection syringe for in-

281   situ nitrogen cycling experiments. Results are reported from two of these chambers (SDRO and

282   NDT3-D) and all $^{15}N-NO_3^-$ chambers were excluded from benthic flux calculations (see next

283   section).

284

285   **2.8 In Situ ^{15}N Incubations**

286   Two hundred μmol of ^{15}N-labeled potassium nitrate (99% ^{15}N; Cambridge Isotopes) was injected

287   into the ^{15}N incubation chamber at each site to obtain a final concentration of ~50 – 100 μM ^{15}N-

288   labeled nitrate. Nitrate was amended at this level to prevent its depletion before the last sampling

289   time point (Valentine et al., 2016). Samples for $\delta^{15}N$ analysis were preserved by filling a pre-

290   vacuumed 12-ml exetainer vial with 0.1 ml 7M zinc chloride as a preservative. Another aliquot

291   (~12 ml) of seawater for ammonium isotope analysis (see section 2.7.2) was filtered through 0.2

292   μm syringe filters and stored frozen. Prior to analyzing the samples in 12-ml exetainer vials, 5

293   mL of sample was replaced with ultra-high purity helium to create a headspace. The

294   concentration and $\delta^{15}N$ of dissolved N_2 and N_2O was determined using a Sercon CryoPrep gas

295   concentration system interfaced to a Sercon 20-20 isotope-ratio mass spectrometer (IRMS) at the

296   University of California Davis Stable Isotope Facility.

297

298   **2.9 Ammonium Isotope Analyses**

299   The production of $^{15}NH_4^+$ in seawater samples was measured using a method adapted from

300   (Zhang et al., 2007) and described previously by (Peng et al., 2016). In brief, NH_4^+ was first

301   oxidized to NO_2^- using hypobromite (BrO^-) and then reduced to N_2O using an acetic acid-azide

302   working solution (Zhang et al., 2007). The $\delta^{15}N$ of the produced N_2O was determined using an

303   Elementar Americas PrecisION continuous flow, multicollector, isotope-ratio mass spectrometer

304   coupled to an automated gas extraction system as described in (Charoenpong et al., 2014).

305   Calibration and correction were performed as described in (Bourbonnais et al., 2017). The

306   measurement precision was ±0.2 ‰ for $\delta^{15}N$. Depending on the in-situ ammonium

307   concentration, the detection limit for total NH_4^+ production rates ranged between 0.006 and

308   0.0685 mmol m^{-2} d^{-1}.

309

3. Results

3.1 Bottom water conditions

O_2 and NO_3^- concentrations in the bottom water along the transects can be seen in Table 1. O_2 concentrations below detection as determined by the ROV sensor could in some cases be considered to represent anoxia (0 μM O_2) based on a set of different analytical methods (see discussion section 4.1). Bottom water solute concentrations (as defined by the average T_0 concentration in BFC at each site) can be seen in Suppl. Figs. 1-4. Bottom water NO_3^- concentrations roughly decreased with station depth (e.g., 28 μM at NDT3-D vs. 19 μM at NDRO). Bottom water NO_2^- concentrations were below detection at all stations. Bottom water NH_4^+ concentrations were 9 μM at NDRO and 13 μM at SDRO and below detection in shallower stations. Bottom water PO_4^{3-} concentrations roughly increased with increasing basin depth (e.g., 2 μM at SDT3-D vs. 7 μM at SDRO). Finally, Fe^{2+} was 2 and 5 μM at the NDRO and SDRO stations, respectively and below detection at all shallower stations.

3.2 Sediment characteristics

Photographs of sediment cores with a depth scale are shown below Table 1. Sediment colors were classified according to (Hossain et al., 2014). Cores from the shallowest (D) stations were uniformly reddish in color with small pockets of black. The sediment color changed with station depth, transitioning from a reddish color in the shallowest stations to predominantly black with reddish laminations at the depocenter stations. The band of black sediment appeared at approx. 8 cm sediment depth in the C-station cores and became progressively more ubiquitous with station depth. Notably, NDT3-C sediment (Table 1B) contained black bands from approx. 6-14 cm sediment depth, while SDT3-C sediment (Table 1J) had a much narrower band around 8-10 cm.

Sediment cores from shallower stations (D and C stations) contained signs of bioturbation (e.g.,

u-shaped burrows) and, in some cases, contained visible macrofauna, such as polychaetas and

mollusks. Deeper in the basin (A and depocenter stations) no signs of bioturbation were detected,

Table 1. Station details and photos of representative ROV push cores taken at each station. Mat presence (Y = yes, N = no) was determined visually. Station water depth and oxygen concentration were determined by sensors attached to ROV Jason (bdl = below detection limit (<3 µM O_2). Anoxia was confirmed by additional methods (see discussion section 4.1). Latitude and longitude were determined by triangulation between the ROV and the ship. Bottom water nitrate concentration was derived from an average of benthic flux chamber nitrate measurements at time 0 for each station (chambers with no calculatable flux and ^{15}N-nitrate addition excluded). Note, benthic flux chambers were not deployed at SDT1-A. Photographs show the sediment-water interface (SWI; top part) and each sediment core in full length (lower part).

Parameter	NDT3-D	NDT3-C	NDT3-B	NDT3-A	NDRO	SDRO	SDT1-A	SDT3-A	SDT3-B	SDT3-C	SDT3-D
Mat Present	N	N	N	Y	Y	Y	Y	Y	N	N	N
Depth (m)	447	498	537	572	580	586	573	571	536	494	447
Latitude (°)	34.363	34.353	34.333	34.292	34.262	34.201	34.212	34.184	34.168	34.152	34.142
Longitude (°)	-120.015	-120.016	-120.019	-120.026	-120.031	-120.044	-120.116	-120.047	-120.053	-120.050	-120.052
Oxygen (µM)	8.7	5.2	12.2	9.2	0.0	0.0	0.0	0.0	1.8	3.1	9.6
Nitrate (µM)	27.3	26.0	11.5	24.4	18.5	9.9		20.4	20.6	16.3	28.0
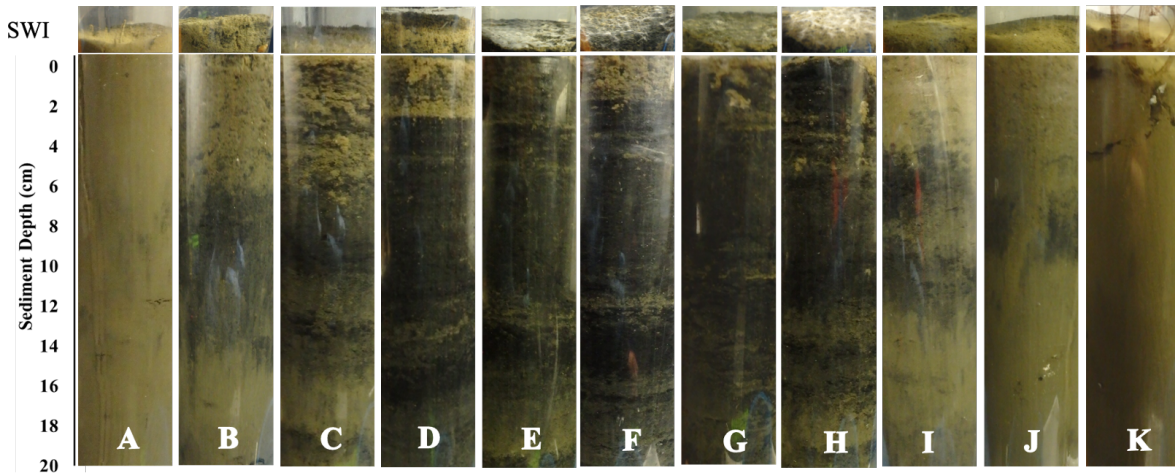
and the sediment-water interface was colonized by patches of white GSOB mats. Spherical cells

(given the moniker 'ghost balls') were found mixed amongst giant sulfur bacteria filaments

within the top 0-1 cm of sediment at NDRO (Suppl. Fig. 7). These unknown species had similar

morphological characteristics to the species *Thiomargarita namibiensis* (Schulz et al., 1999;

Schulz and Schulz, 2005) containing a translucent cell with sulfur granules giving them a ghostly

white appearance. A small sample of cells (n = 8) were measured, featuring diameters between

48.0 and 99.6 µm, amounting to an average biovolume of 2.5 x 10^5 µm^3, compared to *T.*

namibiensis with a cell diameter usually between 100-300 µm (Schulz et al., 1999).

Table 2. Sediment solid phase data: porosity, density, total organic carbon (TOC), total organic nitrogen (TON), C:N ratio, and δ13C. All data were averaged for the top 0-19 cm sediment, except NDT3-C (17 cm), NDT3-A (11 cm) and SDRO (7 cm), where the core length was shorter. Integrated sulfate reduction rates (iSRR) were integrated over 0-14 cm sediment depth. No sulfate reduction rates are available for NDT3-B, SDT3-A, and SDT3-B; rates were not integrated for SDRO due to missing surface samples.

Parameter	NDT3-D	NDT3-C	NDT3-B	NDT3-A	NDRO	SDRO	SDT1-A	SDT3-A	SDT3-B	SDT3-C	SDT3-D
Porosity	0.79 ± 0.03	0.81 ± 0.04	0.86 ± 0.04	0.88 ± 0.03	0.88 ± 0.04	0.87 ± 0.03	0.88 ± 0.03	0.86 ± 0.04	0.85 ± 0.04	0.82 ± 0.04	0.78 ± 0.04
Density	1.21 ± 0.07	1.16 ± 0.08	1.06 ± 0.08	1.05 ± 0.04	1.06 ± 0.03	1.04 ± 0.03	1.11 ± 0.23	1.05 ± 0.05	1.12 ± 0.06	1.22 ± 0.05	1.22 ± 0.03
TOC (%)	2.9 ± 0.5	2.5 ± 0.5	3.6 ± 0.5	3.1 ± 0.4	3.3 ± 0.4	3.5 ± 0.4	4.5 ± 0.5	3.2 ± 0.0	3.6 ± 0.6	3.6 ± 0.8	3.3 ± 0.5
TON (%)	0.3 ± 0.1	0.5 ± 0.1	0.4 ± 0.1	0.4 ± 0.1	0.4 ± 0.0	0.4 ± 0.1	1.0 ± 0.1	0.4 ± 0.0	0.4 ± 0.1	0.4 ± 0.1	0.4 ± 0.1
C:N Ratio	8.9 ± 0.2	8.7 ± 0.5	8.5 ± 0.5	8.2 ± 0.2	8.2 ± 0.4	8.0 ± 0.2	8.6 ± 0.8	8.3 ± 0.6	8.3 ± 0.3	8.7 ± 0.3	8.5 ± 0.2
δ^{13}C (‰)	-22.4 ± 0.3	-22.4 ± 0.4	-22.2 ± 0.4	-22.1 ± 0.2	-22.1 ± 0.2	-22.0 ± 0.3	-21.3 ± 0.7	-22.1 ± 0.4	-22.0 ± 0.2	-21.9 ± 0.2	-22.0 ± 0.1
Integrated SRR (mmol m^{-2} d^{-2})	2.9	3.8		2.7	4.1		2.9			1.7	1.9

B station cores contained sporadic GSOB filaments slightly deeper in the sediment (approx. 2-4

cm sediment depth). Sediment solid phase parameters (averaged over the entire sediment core

depth) can be seen in Table 2. Average sediment porosity increased with basin depth (e.g., from

0.79 at NDT3-D to 0.88 at NDRO). TOC, TON, the C/N ratio, and the δ^{13}C isotopic signature of

organic carbon remained relatively constant (2.5 – 4.5%, 0.1 – 0.4%, 8.0 – 8.7 and 21.3 –

22.4 ‰, respectively) over all stations.

3.3 Sediment porewater geochemistry

Total alkalinity (Figs. 2 A-E & 3 A-F) increased steadily with sediment depth at all stations

starting with, on average, 2.4 mM in the core supernatant reaching a maximum at the respective

deepest sediment sample (20 cm). Porewater alkalinity and DIC also increased with basin depth

377 (Figs. 2 A-E & 3 A-F) indicating that total alkalinity was dominated by the carbonate system.

378 Porewater DIC was, on average, 2.2 mM in the core supernatant and reached maximum

379 concentrations at the deepest sediment depth (20 cm) at most stations.

380

381 Porewater PO_4^{3-} profiles (Figs. 2 A-E & 3 A-F) were markedly different between the depocenter

382 and shallower C and D stations. Porewater PO_4^{3-} concentrations in the depocenter and A stations

383 generally increased with sediment depth but several profiles (NDT3-C, NDT3-A, SDRO, SDT1-

384 A) remained unchanged or decreased deeper in the sediment (starting at approx. 10 cm). The

385 profiles in C and D stations showed a peak in PO_4^{3-} concentrations near the sediment-water

386 interface, particularly in the northern basin. Below 2 cm, PO_4^{3-} decreased with sediment depth,

387 but sometimes showed a second small peak deeper in the sediment (12-14 cm at NDT3-D and

388 10-12 cm at SDT3-D).

389

390 Porewater NH_4^+ concentrations (Figs 2 & 3 A-E) showed trends often similar to alkalinity and

391 DIC; NH_4^+ concentrations increased downcore and were higher at depocenter than at D stations

392 (e.g., 370 and 91 µM at 20 cm for SDRO and SDT3-D, respectively). Porewater NO_2^- (Suppl.

393 Table 1) and NO_3^- (Figs. 2 F-J & F G-L) concentrations were at or near zero below 2 cm at every

394 station, except at SDRO and NDT3-A where large peaks in NO_3^- (376 and 81 µM, respectively)

395 and NO_2^- (37 and 5 µM, respectively) occurred in the top 1 cm.

396

397 Porewater Fe^{2+} concentrations (Figs. 2 F-J & 3 G-L) were several orders of magnitude higher at

398 shallower D-stations (max. 722 and 395 µM at NDT3-D and SDT3-D, respectively) compared to

399 depocenter stations (max. 13 and 51 µM at NDRO and SDRO, respectively). NDT3-C porewater

400   Fe^{2+} concentration (Fig. 2G) peaked in the top 1 cm of sediment (similar to deeper stations)

401   while SDT3-C porewater Fe^{2+} concentration (Fig. 3H) peaked around 5-cm sediment depth. Fe^{2+}

402   concentrations reached a max. at 0-2 cm and declined sharply with depth in depocenter and A-

403   station sediment. Northern basin sediment was similar, but the decline in Fe^{2+} below 0-2 cm was

404   less pronounced.

405

406   Maximum porewater sulfide concentrations (Figs. 2 F-J & 3 G-L) were several orders of

407   magnitude lower at the shallower D-stations (5 and 4 µM at NDT3-D and SDT3-D, respectively)

408   compared to A stations (350 and 148 µM at NDT3-A and SDT1-A, respectively). Unlike Fe^{2+},

409   peaks in sulfide concentration occurred deeper in the sediment (e.g., below 5 cm depth at A

410   stations). Porewater sulfate concentrations (Figs. 2 K-O & 3 M-R) decreased slightly with depth,

411   but never reached values below 20 mM at any station.

412

413   **3.4 In-situ microprofiling**

414   Microprofiler O_2 and sulfide measurements are shown in Fig. 4. Oxygen was rapidly consumed

415   within the first 0-1 cm of sediment at every station where O_2 was detected in the bottom water

416   (i.e., at all stations except NDRO, which showed no positive signal of oxygen in the water

417   compared to the sediment; note that no oxygen profile is available for SDRO). Sulfide

418   concentrations from microsensors showed similar trends to spectrophotometric measurements,

419   albeit with different absolute values (below detection in shallower B-, C- and D-stations that

420   lacked mats and >1,000 µM at A- and depocenter stations). Microprofiler pH (Fig. 4) was near

421   7.5 in the bottom water at all stations, and slowly decreased to near 7.0 in the lower parts (3-5

cm) sediment at most stations except NDT3-C and SDT3-B. pH at 2.5 cm at SDT3-B reached

6.77, which was the lowest observed during this expedition.
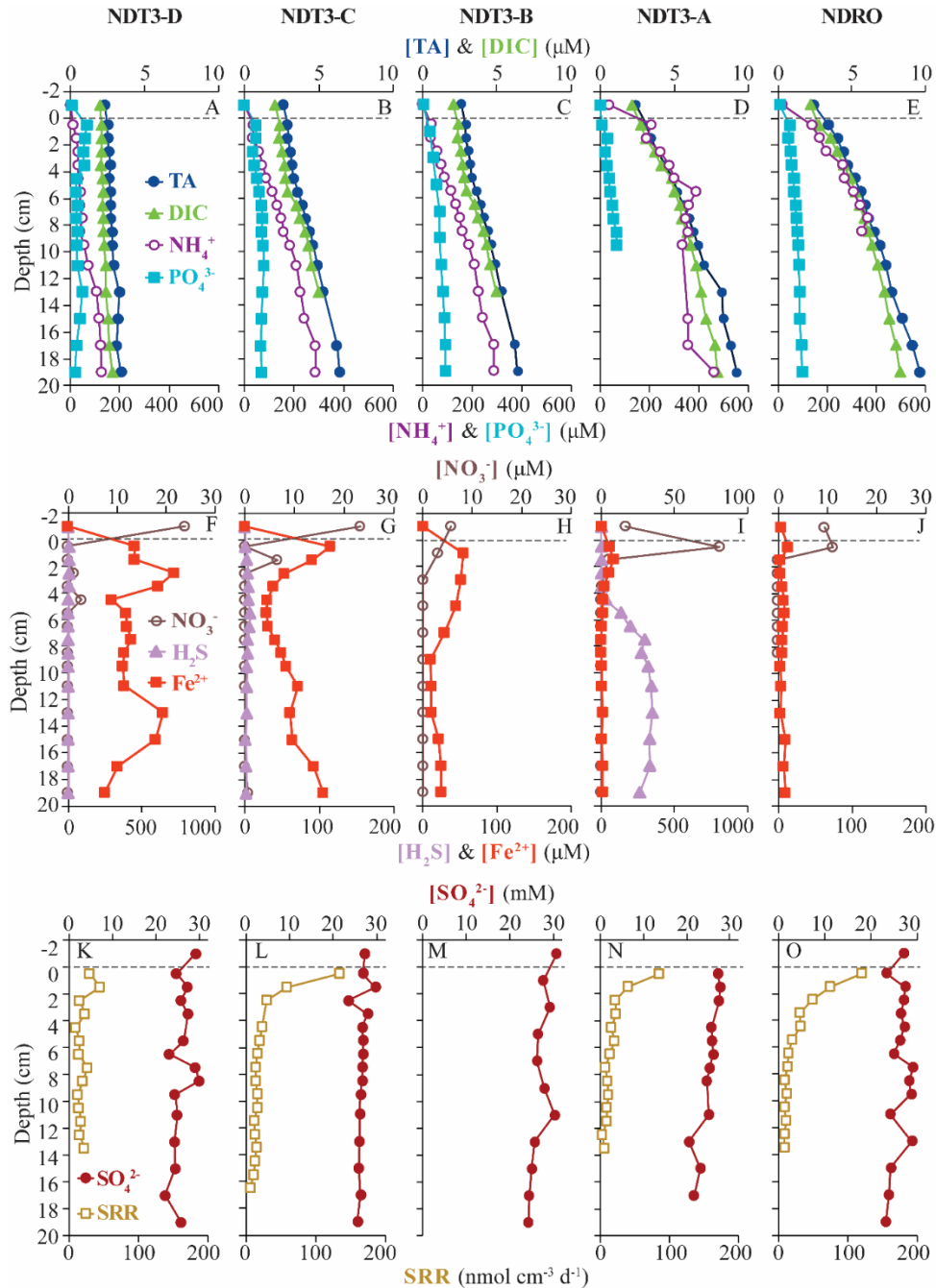
Figure 2. Biogeochemical data from ROV sediment push cores collected at stations on the northern transect (NDT3) and in the northern depocenter (NDRO): total alkalinity (TA), dissolved inorganic carbon (DIC), ammonium (NH$_4^+$), phosphate (PO$_4^{3-}$) in the first row; nitrate (NO$_3^-$), total sulfide (sulfide), and iron (II) (Fe^{2+}) in the second row; sulfate (SO$_4^{2-}$) and bacterial sulfate reduction rate (SRR) in the third row. Data analyzed from sediment core supernatant are plotted at -1 cm sediment depth; the dotted line connotes the sediment-water

21

interface. Note the change in scale on the primary x-axis in panel I and the change in scale of the secondary x-axis in panels F and I. No spectrophotometric sulfide data is available for NDRO and NDT3-B and no SRR data is available for NDT3-B. For station details see Fig. 1 and Table 1.
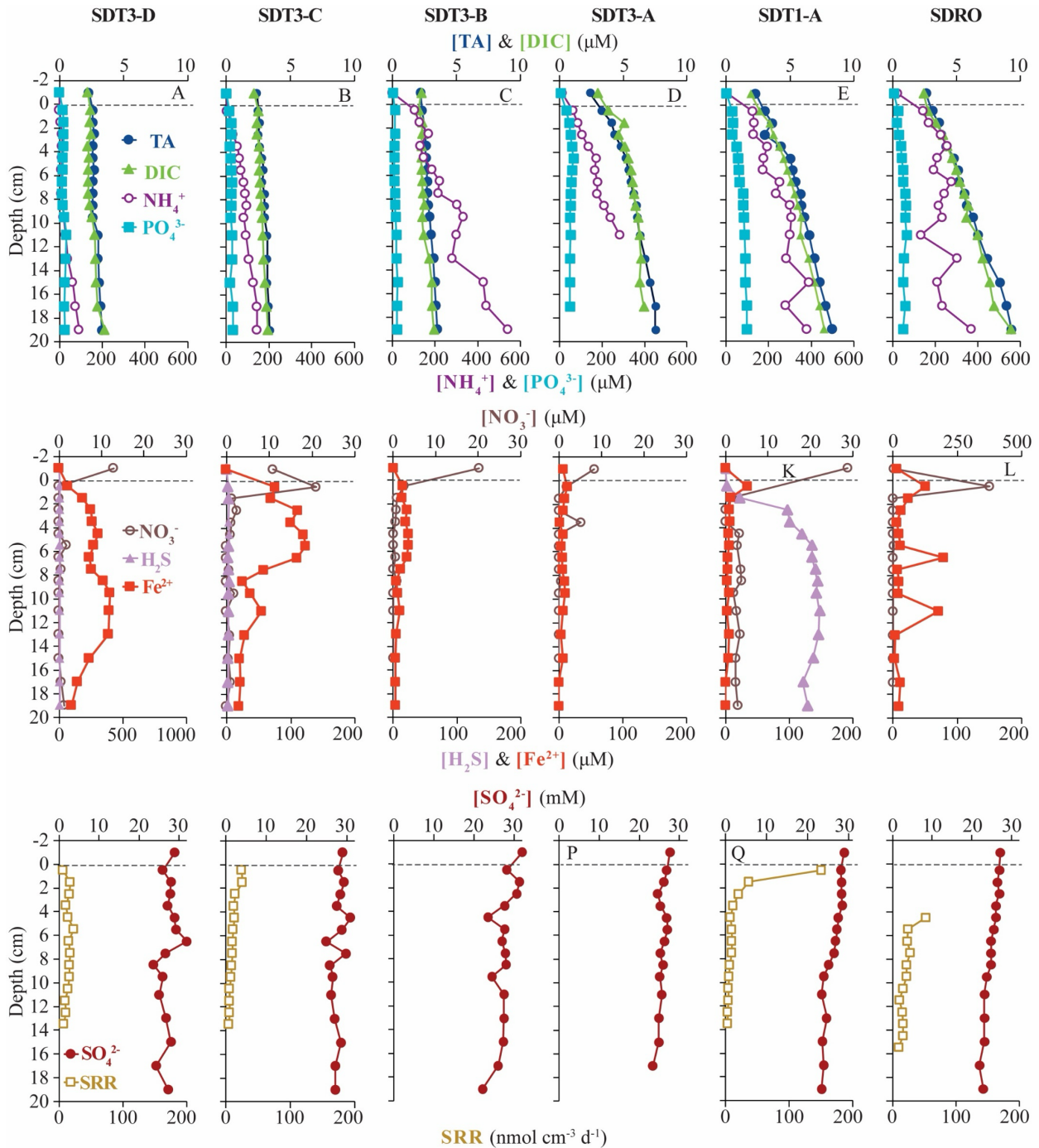
Figure 3. Biogeochemical data from ROV sediment push cores collected at stations on the two southern transects (SDT1 and SDT3) and the southern depocenter (SDRO): total alkalinity (TA), dissolved inorganic carbon (DIC), ammonium (NH_4^+), phosphate (PO_4^{3-}) in the first row; nitrate (NO_3^-), total sulfide (sulfide), and iron (II) (Fe^{2+}) in the second row; sulfate (SO_4^{2-}) and bacterial sulfate reduction rate (SRR) in the third row. Data analyzed from sediment core supernatant are plotted at -1 cm sediment depth; the dotted line connotes the

441 sediment-water interface. Note the change in scale on the primary x-axis in panel L and the change in scale of
442 the secondary x-axis in panel G. No sulfide nor SRR data are available for SDT3-B and -A; spectrophotometric
443 sulfide data and the top 0-4 cm of SRR data are not available for SDRO. For station details see Fig. 1 and Table
444 1.

445
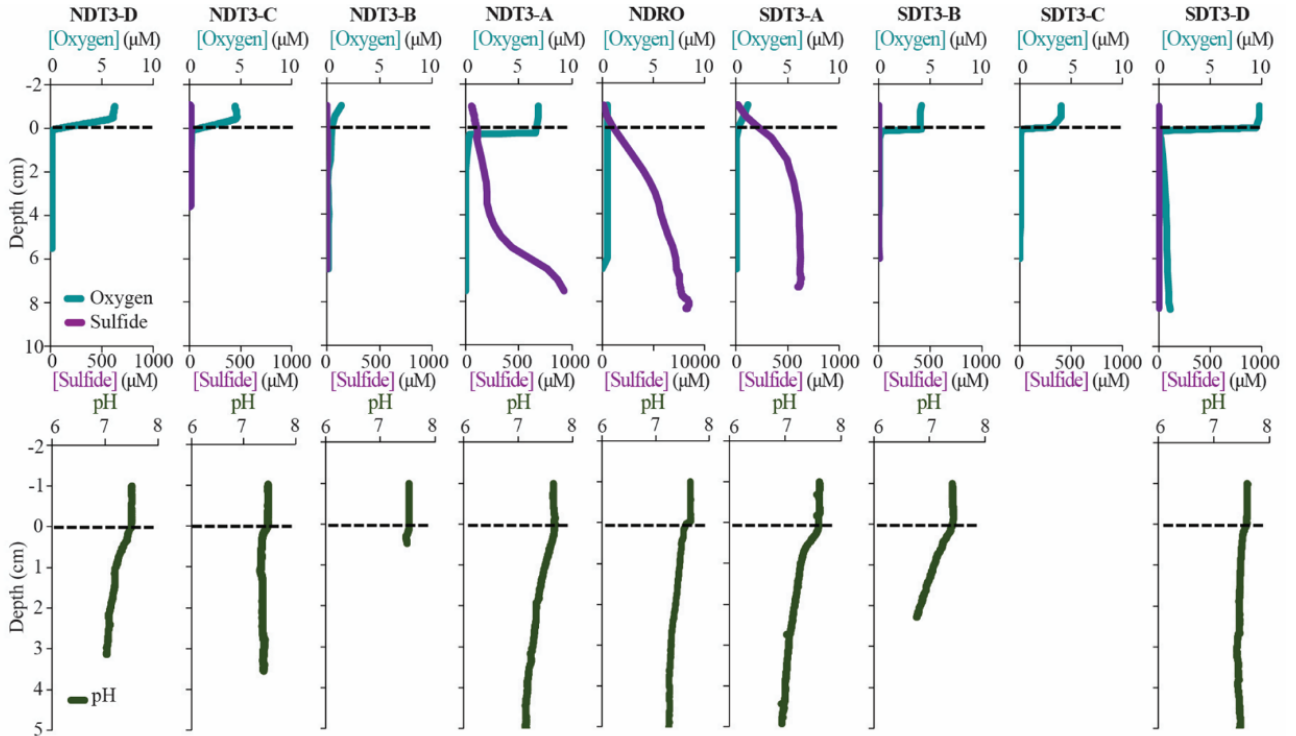
446
447
Figure 4. In-situ sediment microprofiler results for all stations (except SDT1-A and SDRO): oxygen (O_2) and
449 total sulfide (sulfide) concentration in the first row; pH profiles in the second row. Note the change in scale on
450 the secondary x-axis for NDRO sulfide. Values determined in the overlying water are plotted at negative
451 sediment depths; the dotted line connotes the sediment-water interface.

452

3.5 In-situ fluxes of benthic solutes

454 NO_3^-, NH_4^+, PO_4^{3-}, and Fe^{2+} flux measured in the BFC revealed different patterns of uptake and

455 release from the sediment throughout the basin (Fig. 5 and Suppl. Figs. 1-4). BFC O_2

456 concentrations were compromised by O_2 release from the chamber's polycarbonate walls, which

457 prevented an accurate calculation of O_2 fluxes from BFC sensor data. NO_3^- was consumed at all

458 stations as indicated by a negative flux (i.e., a flux into the sediment). On the contrary, benthic

459 release (i.e., a flux out of the sediment) was observed for all other analyzed solutes (NH_4^+, PO_4^{3-},

23

460 and Fe^{2+}), with the lowest fluxes in the shallow D and C-stations and highest fluxes in the

461 depocenter. Ammonium fluxes were the highest of all the determined solutes and showed the

462 largest difference between deep and shallow stations, with a flux of 1.6 mmol m^{-2} d^{-1} at NDT3-C

463 (there were no measurable NH_4^+ fluxes in D-station chambers) and reaching 11.1 ± 3.1 mmol m^{-2}

464 d^{-1} (n = 3) at the two depocenter stations. The depocenter ammonium flux far-outpaced the

465 concomitant flux of nitrate into depocenter sediments (-3.2 $\pm$ 0.7 mmol m^{-2} d^{-1}, n = 3). Iron and

466 phosphate fluxes were similar at depocenter stations (4.1 $\pm$ 0.7, n = 3, and 3.2 $\pm$ 0.7, n = 3, mmol

467 m^{-2} d^{-1}, respectively). Alkalinity and DIC concentrations from flux chambers (Suppl. Figs. 5 and

468 6) remained constant at all stations and thus no DIC flux was calculated. Results from BFCs

469 injected with ^{15}N-NO_3^- at the SDRO and NDT3-D station are shown in Fig. 6. The rates of

470 denitrification, anammox, and N_2O production were higher at SDRO compared to NDT3-D.

471 $^{15}NH_4^+$ production (DNRA) was one order of magnitude higher at the SDRO station (2.67 mmol

472 m^{-2} d^{-1}) compared to the NDT3-D station (0.14 mmol m^{-2} d^{-1}). DNRA accounted for a much

473 higher percentage of NO_3^- reduction at SDRO (54.1%) than NDT3-D (13.3%).

474

475 **3.6 Sulfate reduction rates**

476 Vertical profiles of bacterial sulfate reduction as determined by the radioisotope technique

477 differed throughout the basin (Figs. 2 & 3). Peaks in sulfate reduction were seen in the top 0-1

478 cm of sediment at stations with a visible GSOB mat on the surface (120.2, 151.0, and 85.3 nmol

479 cm^{-3} d^{-1} at NDRO, SDT1-A, and NDT3-A, respectively). Sediments at most shallower basin

480 depths exhibited peaks slightly deeper in the sediment and of lower magnitude (25.5, 44.5, 22.5

481 nmol cm^{-3} d^{-1} at SDT3-C, NDT3-D, and SDT3-D respectively). NDT3-C had no visible GSOB

482 mats but exhibited a peak (133.7 nmol cm^{-3} d^{-1}) in sulfate reduction at 0-1 cm depth, similar to

483   deeper stations (e.g., NDRO in Fig. 2O), which differed from other shallow stations (e.g., SDT3-

484   C in Fig. 3N). The integrated sulfate reduction rate (0-14 cm depth) at NDRO (4.1 mmol m^{-2} d^{-1})

485   was noticeably higher than most other stations with the exception of NDT3-C (3.8 mmol m^{-2} d^{-1})

486   (Table 2). NDT3-D and NDT3-C exhibited higher integrated rates (2.9 and 3.8 mmol m^{-2} d^{-1})

487   than their southern station counterparts SDT3-D and SDT3-C (1.9 and 1.7 mmol m^{-2} d^{-1}).

488
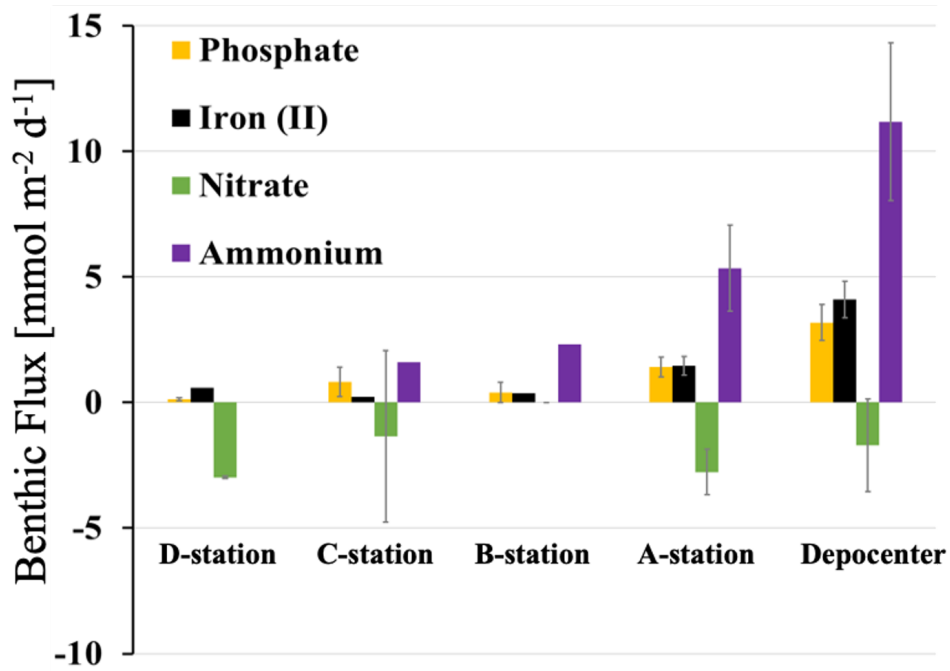
Figure 5. Benthic fluxes of solutes (positive flux = release from the seafloor; negative flux = uptake by the seafloor) determined with in-situ benthic flux chambers. Rates were averaged for stations of same depth from the northern and southern transect and the depocenter (NDRO and SDRO). Note, giant sulfur-oxidizing bacterial mats were found at depocenter and A-stations. Error bars represent standard errors.
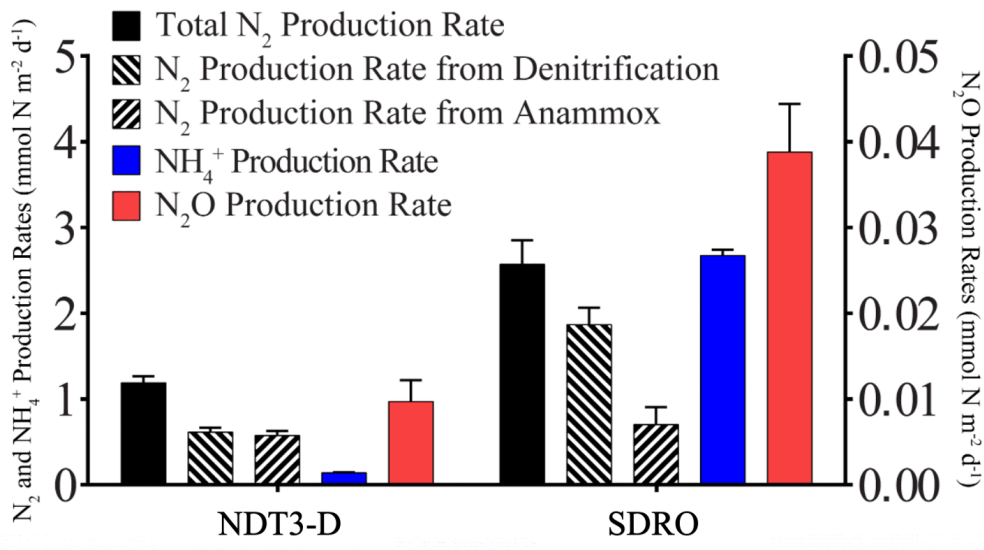
Figure 6. Areal rates of total N_2 production, denitrification, anammox, NH_4^+ production (DNRA), and N_2O production

4. Discussion

4.1 Giant sulfur-oxidizing bacterial mats proliferated in response to deoxygenation in the Santa Barbara Basin

The SBB is an ideal environment to study the effect of transient deoxygenation on benthic biogeochemistry. In Fall 2019, when this expedition took place, the SBB was undergoing a transition from oxygenated to virtually anoxic conditions (Qin et al., 2022). When the AT42-19 cruise occurred, most of the bottom water in the basin was hypoxic (A-, B-, C-, and D-stations), except for the depositional center. Separate O_2 measurements from the ROV sensor (O_2 below detection limit, Table 1), microprofilers (no signal change between water column and sediment, Fig. 4), and Winkler titration from CTD/rosette casts (uniform non-zero value below 500 m (Qin et al., 2022)) indicated full anoxia in the bottom water at the deeper stations (NDRO and SDRO). Notably, bottom water conditions revealed a slight asymmetry between the basin transects (Fig. 1); bottom water along the northern transect generally had more O_2 and NO_3^- than the southern transect (e.g., 9 μM O_2 at NDT3-A and 0 μM O_2 at SDT3-A). This asymmetry indicated differences in the circulation and/or microbial communities between the northern and southern portions of the basin. Whether this asymmetry is a permanent feature of the basin or symptomatic of the specific conditions in November 2019 is unclear; previous studies in the SBB have been restricted to the depocenter or one side of the basin (Sholkovitz, 1973; Reimers et al., 1996a; Kuwabara et al., 1999). Regardless of bottom water oxidant concentration, the energetically most favorable terminal electron acceptors (O_2 and NO_3^-) disappeared in a very narrow zone below the sediment-water interface (Fig. 4 and Figs. 2 and 3, respectively), consistent with their expected rapid consumption by the benthic microbial community.

525   In the present study, benthic GSOB mats were primarily limited to the anoxic depocenter of the

526   SBB. Similarly, such mats were replete in the core of the anoxic Peruvian OMZ (Levin et al.,

527   2002; Sommer et al., 2016; Mosch et al., 2012), but absent from the seafloor below the hypoxic,

528   i.e., slightly oxygenated, Mauritanian OMZ (Schroller-Lomnitz et al., 2019). GSOB mats in

529   November 2019 were observed deeper in the basin than in October 2013 (Valentine et al., 2016)

530   but in a similar location to June 1988 (Reimers et al., 1996a) and April 1997 (Kuwabara et al.,

531   1999). During the 2013 sampling, dense GSOB mats were confined to depths between approx.

532   500-570 m (equivalent to the B-stations from this expedition), corresponding with anoxic

533   conditions in the bottom water. This habitat was sandwiched between an anoxic, anitric (i.e.,

534   nitrate-free) deep and a hypoxic, nitrigenated (i.e., nitrate-rich) shallower water layer (Valentine

535   et al., 2016). The difference in depth distribution of GSOB mats between the 2013 and 2019

536   expedition provides evidence that GSOB mats in the SBB are ephemeral and proliferate where

537   the bottom water is anoxic but not anitric.

538

539   As our study represents only a snapshot of an oxygen- and nitrate-driven mat dynamic, we can

540   only speculate how areas of the basin that did not contain GSOB mats in November 2019 fit into

541   this dynamic. For example, mat-forming sulfur bacteria found slightly deeper in the sediment at

542   B-stations (see section 3.2) could be progenitors to surface sediment colonization of thick GSOB

543   mats, as has been recorded in other transiently deoxygenated environments (Jørgensen, 1977).

544   Alternatively, these subsurface colonies could also be remnants of a former surface GSOB mat

545   that retreated under changing redox conditions. Oxygenated conditions in the water preceding

546   the 2019 expedition would, in this context, suggest the mats migrated following a previous

547   anoxic event (Qin et al., 2022). If deoxygenation persisted in the SBB after the AT42-19 cruise,

548 then anitria (i.e., anitric conditions - similar to anoxia) would likely follow in the deepest basin

549 water. These conditions would be similar to those seen in 2013 (Valentine et al., 2016), where

550 GSOB mats formed a contiguous "donut ring" at shallower basin depths. Interestingly, GSOB

551 mats in the Eastern Gotland Basin of the Baltic Sea were confined to a hypoxic transition zone,

552 where O_2 was < 30 µM but did not reach anoxia, while no mats were observed at deeper anoxic

553 locations (Noffke et al., 2016). This difference in distribution compared to the SBB suggests that

554 GSOB mats proliferate under different conditions (anoxic or hypoxic), potentially depending on

555 the species of mat-forming bacteria present and whether they specialize in aerobic or anaerobic

556 chemosynthesis.

557

558 **4.2 Shift from benthic denitrification to dissimilatory nitrate reduction to ammonium in**

559 **response to complete deoxygenation in the Santa Barbara Basin**

560

561 Benthic uptake and release of nitrogen species by SBB sediment appeared to be affected by the

562 presence of GSOB mats. While total benthic nitrate uptake was similar between D- and

563 depocenter stations based on in-situ NO_3^- flux measurements (Fig. 4), NH_4^+ release from the

564 sediment into the water column increased where GSOB mats were present (Fig. 5). This trend is

565 supported by the porewater profiles of NH_4^+, which showed a steeper increase over sediment

566 depth at deeper stations (Figs. 2 & 3). Incubations with ^{15}N-NO_3^- revealed that N_2 production

567 (denitrification and anammox) accounted for 86% of NO_3^-/NO_2^- reduction in the shallow basin,

568 while NH_4^+ production (DNRA) accounted for 13% and N_2O production accounted for 1%

569 (NDT3-D, Fig. 6;(Peng et al., 2023)). In contrast, most (54%) of NO_3^- reduction at the

570 depositional center occurred via DNRA; N_2 production accounted for 45% and N_2O production

571   accounted for 1% of NO_3^- reduction at the SDRO (Fig. 6; Peng et al. 2023). It is important to

572   note that these results only describe patterns of NO_3^- reduction in the basin, while other

573   mechanisms of nitrate uptake by sediment (e.g., hyper-accumulation of nitrate into vacuoles) are

574   more difficult to calculate accurately. It is also important to note that diatoms hyper-accumulate

575   nitrate (Kamp et al., 2011) and meiofauna (e.g., nematodes) can positively impact rates of

576   denitrification (Bonaglia et al., 2014). Both diatoms and meiofauna were seen in SBB depocenter

577   and A-station sediments in November 2019 (data not shown), so their impact on SBB benthic

578   nitrogen cycling is likely important and remains to be disentangled from the mats themselves.

579

580   This data suggests a transition from denitrification-dominated sediment in the oxygenated basin

581   to an increasing influence of DNRA on N cycling in the deeper, anoxic basin. Placed in the

582   context of other OMZs, Mauritanian shelf sediment was dominated by denitrification (Dale et al.,

583   2014), similar to SBB shallow sediment (below hypoxic water) while core Peruvian OMZ

584   sediment was dominated by DNRA, similar to sediment of the deeper SBB (below anoxic water)

585   (Sommer et al., 2016). Nitrate reduction in sediment below the seasonally hypoxic Eckernförde

586   Bay (Dale et al., 2011) and below the hypoxic transition zone of the Eastern Gotland Basin

587   (Noffke et al., 2016) also showed increased DNRA where GSOB mats were present, though with

588   an order of magnitude lower NH_4^+ flux (avg. 1.74 mmol m^{-2} d^{-1} and max. 1.10 mmol m^{-2} d^{-1},

589   respectively) than the SBB depocenter.

590

591   While our study suggests a shift from denitrification to DNRA during deoxygenation of SBB

592   bottom water, other studies examined changes in benthic nitrogen cycling under reverse

593   conditions, i.e., the reoxidation of the environment following anoxia (Hylén et al., 2022; De

594 Brabandere et al., 2015). After a decadal oxygenation event in the Eastern Gotland Basin (Baltic

595 Sea) in 2015-2016, sediment exhibited a slight increase in denitrification, but remained

596 dominated by DNRA and N_2O production (Hylén et al., 2022). The lack of N_2 production via

597 denitrification following this oxygenation event was attributed to the reoxygenation event being

598 too weak to substantially oxidize sediments, which would favor denitrification (Hylén et al.,

599 2022). In an engineered reoxygenation event of the By Fjord on Sweden's western coast, where

600 dissolved O_2 and NO_3^- content of anoxic and anitric bottom water was artificially increased to

601 approx. 130 μM O_2 and 20 μM NO_3^- over a period of roughly 2 years, denitrification rates were

602 increased by an order of magnitude and DNRA rates were also stimulated (De Brabandere et al.,

603 2015). Comparing our results to these two studies suggests that DNRA bacteria are more

604 resilient to weak reoxygenation events and thrive in transiently deoxygenated systems that

605 remain hypoxic ($O_2 < 63$ μM). The frequency and magnitude of reoxygenation and

606 deoxygenation of SBB bottom waters, and the effect of these processes on the benthic microbial

607 community, could be a major factor supporting some of the highest recorded total nitrate

608 reduction rates in a natural benthic marine setting (Peng et al., 2023).

609 **Table 3.** Example reactions of nitrate reduction pathways with associated energy yield in respect to the electron
610 donor (H_2 or HS^-) and electron acceptor (NO_3^-) and electron accepting capacity. Modified from Table 2 in (Tiedje
611 et al., 1983).

Reaction	$\Delta G^{o'}$ (kcal mol^{-1})		Electrons per NO_3^-
	H_2 / HS^-	NO_3^-	
Chemoheterotrophic Denitrification			
$2NO_3^- + 5H_2 + 2H^+ \rightarrow N_2 + 6H_2O$	-53.6	-133.9	5
Chemoautotrophic Denitrification			
$8NO_3^- + 5HS^- + 3H^+ \rightarrow 5SO_4^{2-} + 4N_2 + 4H_2O$	-177.9	-111.2	5
Chemoheterotrophic DNRA			
$NO_3^- + 4H_2 + 2H^+ \rightarrow NH_4^+ + 3H_2O$	-35.8	-143.3	8
Chemoautotrophic DNRA			
$NO_3^- + HS^- + H^+ + H_2O \rightarrow NH_4^+ + SO_4^{2-}$	-107.0	-107.0	8

612

613

614   A high ratio of electron donor to electron acceptor favors DNRA over denitrification (Marchant

615   et al., 2014; Hardison et al., 2015; Tiedje et al., 1983) and this ratio appears to be critical in

616   determining the dominant nitrate reduction pathway in SBB sediments, similar to the Eastern

617   Gotland Basin (Hylén et al., 2022) and the By Fjord (De Brabandere et al., 2015). Example

618   energy yields for denitrification and DNRA are shown in Table 3. As discussed in (Tiedje et al.,

619   1983), heterotrophic denitrification yields more energy per mol of electron donor than DNRA.

620   However, the reverse is true when considering energy yield per mol of electron acceptor (NO_3^-).

621   DNRA also yields 3 more electrons per molecule of NO_3^- than denitrification. Tiedje et al.

622   argued that in environments that are starved of powerful terminal electron acceptors, such as

623   anoxic, organic-rich sediment, the energy yield per electron acceptor and additional electrons

624   available for transfer could push nitrate reduction towards DNRA. Multiple laboratory and

625   model studies have converged on an electron donor to acceptor ratio of approximately 3 to

626   encourage DNRA over denitrification (Hardison et al., 2015; Algar and Vallino, 2014) though

627   other studies have found higher values (Porubsky et al., 2009; Kraft et al., 2014). Sulfide

628   concentrations near the sediment-water interface at the SBB depocenter (approx. 200 µM at 0.5

629   cm depth; Fig. 3, NDRO) would favor chemoautotrophic DNRA over denitrification at ambient

630   marine nitrate concentrations (approx. 28 µM). Additionally, DNRA appears to be the preferred

631   nitrate reduction pathway for chemoautotrophs that utilize iron or sulfide as an electron donor

632   (Caffrey et al., 2019; Kessler et al., 2019; An and Gardner, 2002). As GSOB mats hyper-

633   accumulate nitrate from the bottom water into their intracellular vacuoles, the resulting decline in

634   electron acceptors at the sediment-water interface coupled with an elevation of the sulfate

635   reduction zone would create an electron donor to acceptor ratio that favors DNRA. Since GSOB

636   mats in the SBB seem to prefer DNRA, starving the bottom water of electron acceptors coupled

637 with the high sulfate reduction rates could give them a competitive advantage and allow them to

638 proliferate into the largest-yet mapped GSOB mat in Earth's oceans, as seen in other expeditions

639 (Valentine et al., 2016; Reimers et al., 1996a; Kuwabara et al., 1999).

640

641 **4.3 Microbial mat proliferation and benthic phosphate remineralization dependent on high**

642 **rates of organic matter degradation in the Santa Barbara Basin**

643

644 Organic carbon content of the benthic environment appears to be a key control on sulfate

645 reduction rates near the sediment-water interface as well as microbial mat proliferation. Sulfate

646 reduction rates in the SBB depocenter are most similar in magnitude and profile (i.e., highest

647 rates found at the sediment-water interface and decline drastically thereafter) to those found in

648 sediments below the transiently deoxygenated portion of the Peruvian shelf (e.g., 4.1 mmol m^{-2}

649 d^{-1} at the SBB NDRO station vs. 2.5-3.8 mmol m^{-2} d^{-1} at 128-144 m water depth on the Peruvian

650 margin (Gier et al., 2016; Treude et al., 2021)). The TOC content of surface sediments in these

651 two regions are both high and within the same order of magnitude (maximum recorded TOC of

652 5.2% at the 0-1 cm margin at the SDT1-A station compared with 7.6% in the Peruvian margin

653 145 m depth (Noffke et al., 2012)). In comparison, sulfate reduction rates in the SBB were at

654 least one order of magnitude lower than found in sediment below the OMZ on the Namibian

655 Shelf, which has much higher TOC contents of >10% (Brüchert et al., 2003; Bremner, 1981).

656 Sulfate reduction rates in the shelf sediments below the Eastern Arabian OMZ were much lower

657 (0.18 – 1.27 mmol m^{-2} d^{-1}) than rates in the SBB depocenter (Naik et al., 2017) despite similar

658 hypoxic to anoxic bottom water conditions. These lower sulfate reduction rates were attributed to

659 the relatively low amount of pelagic primary productivity and ergo benthic organic matter

660   delivery in the Eastern Arabian OMZ compared to other upwelling systems (Naik et al., 2017).

661   The organic matter content of the sediment appears to be important in the proliferation of GSOB

662   mats; too much TOC could result in toxic levels of sulfide at the sediment-water interface

663   (*Beggiatoa* exhibit an aversion to sulfidic sediments but toxicity has not been quantified)

664   (Preisler et al., 2007), whereas too little sulfide would not provide enough electron donor for the

665   GSOB's chemoautotrophic metabolism.

666

667   The profiles of several indicators for benthic anaerobic organic matter remineralization (total

668   alkalinity, DIC, PO_4^{3-}, NH_4^+) increased in steepness with increasing water depth (Figs. 2 A-E &

669   3A-F). One divergence from this trend can be seen in PO_4^{3-} profiles from the shallow C- and D-

670   stations, which also featured low rates of sulfate reduction. PO_4^{3-} profiles in these sediments

671   track closely to Fe^{2+} profiles; both solutes dip in concentration in areas with visible iron sulfide

672   formation (e.g., 5-11 cm in NDT3-D as seen in Fig. 2A). Additionally, several stations that

673   exhibited high sulfate reduction rates in surface sediment (e.g., SDT1-A) showed almost no

674   change in PO_4^{3-} at depths below 5 cm (e.g., Fig. 2 K-O compared to Fig. 2 A-E). This

675   phenomenon has been previously documented in SBB sediment and is attributed to the

676   precipitation of carbonate fluorapatite (Reimers et al., 1996a). The confinement of these flat

677   PO_4^{3-} profiles to stations with >100 nmol cm^{-3} d^{-1} sulfate reduction in surface sediment suggests

678   that this mineralogical sink of PO_4^{3-} in SBB sediment may be dependent on high sulfate

679   reduction rates, owing to the bicarbonate produced by sulfate reduction (Reimers et al., 1996a),

680   and is not found throughout the basin. Flat PO_4^{3-} profiles were also reported from the transiently

681   deoxygenated portion of the Peruvian OMZ, where phosphate mineral precipitation has been

682   documented (Noffke et al., 2012). Similar to the shallow margins of the SBB, PO_4^{3-} in

683 Mauritanian OMZ porewater tracks closely with changes in porewater Fe^{2+} (Schroller-Lomnitz

684 et al., 2019), indicating that iron mineralization/dissolution mechanisms hold a greater influence

685 on PO_4^{3-} concentrations under hypoxic bottom waters.

686

687 **4.4 Iron oxide exhaustion is critical for raising the sulfate reduction zone close to the**

688 **sediment-water interface in Santa Barbara Basin sediment.**

689

690 The hyper-accumulation of NO_3^- by GSOB mats potentially facilitates sulfate reduction close to

691 the sediment-water interface in the SBB (e.g., NDRO and NDT3-A as seen in fig. 2N and 2O) by

692 starving the sediment of this more powerful electron acceptor. The rise of the sulfate reduction

693 zone at NDT3-C (fig. 2L) further suggests that the exhaustion of iron oxides and the formation of

694 iron sulfide below the sediment-water interface may play a crucial role in controlling the

695 distribution of sulfate reduction as well. SBB sediments showed a wide vertical and horizontal

696 heterogeneity of redox states based on visual appearance (Fig. 1A-K). Sediment beneath the

697 hypoxic bottom water at the shallowest D-stations was reddish, consistent with a high content of

698 iron oxides. Interestingly, porewater Fe^{2+} concentrations in shallower parts of the basin (e.g.,

699 NDT3-D, max. ~700 μM Fe^{2+}) were an order of magnitude larger than those found in both the

700 Peruvian (max ~60 and ~30 μM Fe^{2+}, respectively; (Noffke et al., 2012; Plass et al., 2020) and

701 Mauritanian (max. ~50 μM Fe^{2+}; Schroller-Lomnitz et al 2019) OMZ. It should be noted that

702 porewater samples for geochemical analyses were unfiltered and hence reported iron

703 concentrations include aqueous, colloidal, and nanoparticulate species. Regardless, all these

704 components represent bioavailable sources of iron. Further, since filtering through 0.45 or 0.2

705 μm filters only removes a fraction of colloidal particles and no nanoparticles (Raiswell and

706 Canfield, 2012), potential surplus porewater iron in SBB samples in comparison to studies that

707 applied filtering was likely minimal.

708

709 Deeper in the basin, bands of black sediment that appear mid-core at NDT3-C (6-14 cm) and

710 SDT3-C (6-10 cm) indicate the formation of iron sulfides as a result of sulfide produced by

711 sulfate reduction (Canfield, 1989). Both D-stations had similar bottom water conditions (Table

712 1), sulfate reduction rates (Fig. 3W-AG), porewater concentrations of solutes (Figs. 2 and 3), and

713 visual sediment characteristics (Section 3.1). On the contrary, there are some noticeable

714 differences in the porewater geochemistry between the two C-stations. At the C-stations, peaks

715 in sulfate reduction were in the surface sediment, above the iron sulfide layers, and declined

716 below approximately 4 cm, indicating a discrepancy between observed peak sulfate reduction

717 activity and the mineralogical clues left behind by the process. Comparing NDT3-C and SDT3-

718 C, iron sulfide formation (Table 1B compared to 1J), porewater Fe^{2+} profiles (Fig. 2G compared

719 to Fig. 3H), and sulfate reduction rates (Fig. 2L compared to Fig. 3N) show that NDT3-C

720 sediment appears to be in transition towards a more sulfidic state, while SDT3-C sediments still

721 mimic the shallow D-station ferruginous state. While sulfate reduction rates for B-stations are

722 not available due to technical issues during sample processing, porewater Fe^{2+} profiles show a

723 similar difference between the north and south basin (Fig. 2H compared to Fig. 3I) as did visual

724 sediment characteristics (Table 1C compared to 1I). This difference in biogeochemical profiles

725 and apparent minerology between the north and south C- and B-stations could be a result of

726 hydrographic and/or bathymetric differences in the basin (Sholkovitz and Gieskes, 1971; Bograd

727 et al., 2002), but a discernable link between the differences in sediment biogeochemistry and the

728 differences in bottom water oxygen (Table 1) need to be further explored.

729

730   Deeper in the basin (depocenter and A-stations), porewater Fe^{2+} concentrations in sediment

731   beneath anoxic bottom water (max. 84 µM Fe^{2+}) were similar to concentrations found below the

732   Peruvian OMZ in 2008 under anoxic bottom water conditions (78 m water depth, max. 80 µM

733   Fe^{2+}) (Noffke et al., 2012). These deep basin porewater Fe^{2+} concentrations were, however, an

734   order of magnitude larger than those found at a similar site on the Peruvian shelf (75 m water

735   depth, max. 1 µM Fe^{2+}) in 2017 during a kelvin-wave-associated "Coastal El Niño" event that

736   created oxygenated bottom waters during the sampling and the disappearance of previously

737   observed dense GSOB mats (Plass et al., 2020). As the SBB water column was undergoing rapid

738   deoxygenation in the weeks preceding this study (Qin et al., 2022), the sediments below the sill

739   appeared to be actively shifting from a ferruginous state to a sulfidic state, with this change

740   starting around the C-stations and being complete in the depocenter. Comparing apparent iron

741   sulfide formation with dips in porewater Fe^{2+} concentrations in C-station profiles (Fig. 1B

742   compared to Fig. 2G and Fig. 1J compared to Fig. 3H) signals a shift away from a ferruginous

743   state occurring just below the SBB sill.

744

745   C-station porewater Fe^{2+} concentrations and sulfate reduction rates indicate that migration of the

746   sulfate reduction zone towards the sediment-water interface is associated with iron sulfide

747   formation deeper in the sediment. The activity (or lack thereof) of cable bacteria, which are able

748   to bridge the gap between the oxidized sediment-water interface and reduced sediment below

749   using a biofilament (Pfeffer et al., 2012), could explain the interplay between sulfate reduction

750   and iron cycling in SBB sediments. Cable bacteria, such as *Ca. Electronema* sp., contain genes

751   involved in DNRA (Kjeldsen et al., 2019) and can perform nitrate reduction in incubation

752 experiments (Marzocchi et al., 2014), but their direct transformation of NO_3^- in the environment

753 appears limited (Kessler et al., 2019) and they appear to be inactive in anoxic aquatic

754 environments (Seitaj et al., 2015; Marzocchi et al., 2018; Hermans et al., 2019). Cable bacteria

755 primarily conduct aerobic sulfide oxidation (Pfeffer et al., 2012), though they can also utilize

756 Fe^{2+} as an electron donor (Seitaj et al., 2015). The maximum recorded filament length of cable

757 bacteria is 7 cm (Van De Velde et al., 2016), though typically they are not stretched completely

758 vertically through the sediment. The appearance of black sediment in the SBB C-station

759 sediments, starting at approx. 5 cm depth, could be an indication that cable bacteria are oxidizing

760 iron sulfides at that sediment depth and prevent their formation at shallower depths. Further,

761 cable bacteria have been found to directly compete with GSOB in transiently deoxygenated

762 systems, with cable bacteria active under oxygenated conditions and GSOB active in anoxic

763 conditions (Seitaj et al., 2015). Cable bacteria can also prevent the benthic release of sulfide,

764 which is toxic to many pelagic animals, via the creation of an iron-oxide buffer (formed through

765 Fe^{2+} oxidation) in near-surface sediments (Seitaj et al., 2015). Therefore, if cable bacteria activity

766 in the SBB decreased with declining oxygen concentrations below the sill, the iron oxide buffer

767 they create could have been reduced, encouraging the sulfate reduction zone to migrate towards

768 the sediment surface (as seen at NDT3-C). Cable bacteria can sometimes be detected in

769 sediments via a slight pH increase (typically pH > 8) (Schauer et al., 2014) which was not

770 reflected in our pH results, but this phenomenon is more typically seen in the laboratory and not

771 the field (Hermans et al., 2019).

772

773 **4.5 Iron and phosphate flux into SBB bottom water is a feature of transient deoxygenation.**

774

775   Release of dissolved iron and phosphate from sediment below anoxic waters is a well-

776   documented phenomenon (e.g., (Mortimer, 1941; Van Cappellen and Ingall, 1994; Van De

777   Velde et al., 2020; Noffke et al., 2012)) and this phenomenon is seen in the SBB as well. As

778   postulated previously (Kuwabara et al., 1999), basin flushing oxidizes iron sulfides at the

779   sediment-water interface, providing ample substrate for microbial iron reduction once anoxia

780   returns. This iron reduction initiates high rates of Fe^{2+} release from SBB depocenter sediment

781   (Fig. 5). Iron reduction further releases iron-bound PO_4^{3-} (Mortimer, 1941) as seen by high

782   benthic fluxes of PO_4^{3-} at the depocenter (Fig. 5), although notably some of this PO_4^{3-} release is

783   likely attributed to organic matter degradation (Van Cappellen and Ingall, 1994). High benthic

784   Fe^{2+} and PO_4^{3-} fluxes were also seen on the Peruvian shelf during transient anoxia (Noffke et al.,

785   2012). The release of these solutes was interpreted to be sourced from a layer of reactive iron

786   hydroxides existing near the sediment surface, likely established during a recent oxygenation

787   event. Similar conditions, i.e., visibly oxidized (reddish) sediment laminae and a thin zone of

788   iron reduction apparent from a peak in Fe^{2+} at the sediment-water interface, were found in

789   sediment from the SBB depocenter. Deeper in the persistently anoxic core of the Peruvian OMZ,

790   sediment appears to have little to no flux of Fe^{2+} and PO_4^{3-} into the bottom water (Noffke et al.,

791   2012). Here, iron at the sediment-water interface is hypothesized to be locked up in iron sulfides,

792   which are rarely re-oxidized due to persistent anoxia.

793

794   In a different study from the Eastern Gotland Basin in the Baltic Sea, enhanced elemental fluxes

795   were observed during a decadal oxygen flushing event (Van De Velde et al., 2020), which was

796   attributed to enhanced elemental recycling, or cycles of mineral precipitation in the water column

797   followed by mineral dissolution once those minerals sink to the sediment. Notably, the iron flux

798   observed in the Eastern Gotland Basin (max. 0.08 mmol m^{-2} d^{-1}) (Van De Velde et al., 2020) was

799   two orders of magnitude lower than the flux observed in the anoxic depocenter of the Santa

800   Barbara Basin (max. 4.9 mmol m^{-2} d^{-1}). It is further notable that benthic fluxes of PO_4^{3-} in the

801   SBB depocenter were also an order of magnitude higher than fluxes in the Eastern Gotland

802   Basin's hypoxic transition zone (3.6 vs. 0.23 mmol PO_4^{3-} m^{-2} d^{-1}) - both of which contained

803   GSOB mats, but while the SBB was anoxic and the Eastern Gotland Basin was hypoxic (Noffke

804   et al., 2016). These differences in Fe^{2+} and PO_4^{3-} flux between the SBB and the Eastern Gotland

805   Basin suggest that reoxidation of the sediment-water interface during basin flushing, as opposed

806   to water-column-associated reoxidation, appears to encourage higher benthic iron fluxes.

807

808   Fe^{2+} and PO_4^{3-} flux from the SBB depocenter were also approximately five times higher (Fig. 5)

809   compared to the anoxic Peruvian shelf (4.9 vs. 0.9 mmol Fe^{2+} m^{-2} d^{-1} and 3.6 vs. 0.8 mmol PO_4^{3-}

810   m^{-2} d^{-1}, respectively) (Noffke et al., 2012). Based on Fe^{2+} profiles, the zone of iron reduction in

811   Peruvian shelf sediments extended down to approx. 10 cm, while the zone appeared to be much

812   shallower and narrower (less than the top 5 cm) in the SBB depocenter. These differences in

813   magnitude of Fe^{2+} concentration and Fe^{2+} and PO_4^{3-} flux between the SBB depocenter and the

814   Peruvian shelf could be attributed to differences in the recency and magnitude of reoxygenation

815   events. The release of Fe^{2+} from sediment into the bottom water could create a buffer against

816   reoxygenation in transiently deoxygenated systems, giving a competitive advantage to anaerobic

817   benthic metabolisms (Dale et al., 2013; Wallmann et al., 2022). Additionally, both Fe^{2+} and

818   PO_4^{3-} release from the SBB sediment could allow for higher rates of primary productivity if

819   those constituents diffused into the photic zone (Robinson et al., 2022). The fate of Fe^{2+} and

820   PO_4^{3-} diffusing into SBB waters from the sediment-water interface is a focus of ongoing work

821   within the basin.

822
823   **5 Conclusions**
824

825   This research expands upon the wealth of science already conducted in the SBB and other

826   transiently deoxygenated environments by examining changes in benthic biogeochemistry

827   promoted by the onset of anoxia. Our main interpretations are summarized in Fig. 7. We found

828   that GSOB mats proliferate in the SBB where the bottom water is anoxic and nitrate

829   concentrations are declining (Fig. 7, A- and depocenter stations). Nitrate uptake by SBB

830   sediment is similar regardless of GSOB mat presence, but these mats appear to initiate a shift

831   from denitrification to DNRA as the primary nitrate reduction pathway (Fig. 7, beginning at B-

832   stations). The zone of sulfate reduction rises to the sediment-water interface where GSOB mats

833   are present (Fig. 7, A-stations), possibly because the hyper-accumulation of nitrate into their

834   intracellular vacuoles starves the environment of this more powerful electron acceptor. However,

835   following the natural order of electron acceptor utilization (Boudreau and Jorgensen, 2001), iron

836   oxides near the sediment-water interface must be exhausted before sulfate reduction can

837   dominate surface sediments and GSOB mats can proliferate in the SBB (Fig. 7, depocenter

838   stations). If anoxic events become longer and more frequent in the SBB because of global

839   warming (see, e.g., (Qin et al., 2022; Stramma et al., 2008)), the iron oxide buffer built up in

840   shallower basin depths could be exhausted, allowing for surface sulfate reduction and the

841   proliferation of GSOB mats in shallower margins of the basin than currently seen. Further, the

842   same transient deoxygenation that allows for these mats to re-stablish themselves also allows for

843   a high Fe^{2+} and PO_4^{3-} flux into the SBB water column. In order to fully understand the complex

844 changes in the benthic environment in response to deoxygenation, genomic and molecular work

845 of the upper sediment community needs to be characterized. Overall, the insights gleaned from

846 this research will aid in the understanding of fundamental biogeochemical changes that occur

847 when marine environments become anoxic.

848
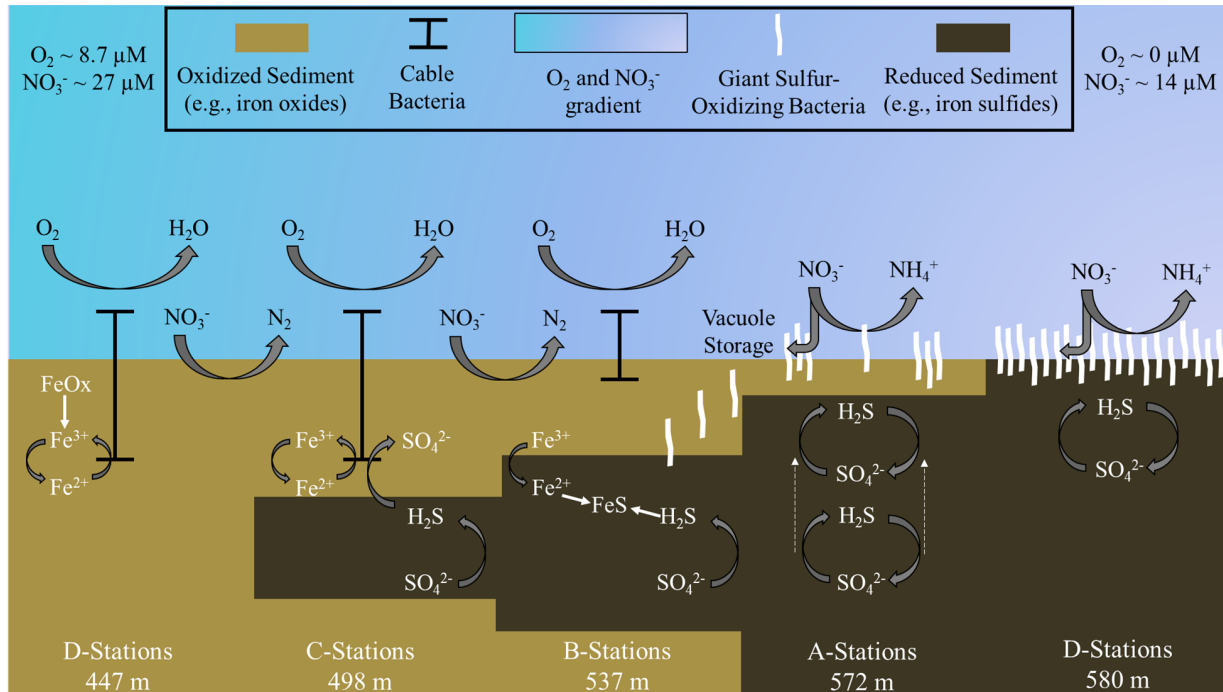
849

850 **Figure 7:** Schematic of biogeochemical processes in the Santa Barbara Basin along the depth gradients
851 studied in October/November 2019. Teal to Lavender gradient represents a decline in O_2 and NO_3^-
852 concentrations with basin depth. In the shallower, hypoxic basin (D-stations), denitrification and iron reduction
853 are dominant and reduced iron is rapidly re-oxidized in near-surface sediment by cable bacteria. Deeper in the
854 basin (A-stations and depocenter), nitrogen cycling shifts towards dissimilatory nitrate reduction to ammonia
855 (DNRA). Reduced iron combines with sulfide, produced by sulfate reduction, diffusing from deeper sediment
856 layers to form iron sulfides. As oxygen concentration approaches zero between the A-stations and the basin's
857 depocenter, giant sulfur-oxidizing bacteria hyper-accumulate nitrate in their intracellular vacuoles. Nitrate
858 removal combined with the exhaustion of available iron oxides in the near-surface sediments allows the zone
859 of sulfate reduction to migrate towards the surface (see dashed arrows at A-stations), providing the giant
860 sulfur-oxidizing bacteria with sufficient reduced sulfur to proliferate into thick, contiguous mats. Note: Figure
861 is not to scale, and processes are simplified to illustrate main concepts.

875

876 **Data availability.**

877 Biogeochemical data presented in this manuscript are accessible through the Biological &

878 Chemical Oceanography Data Management Office (BCO-DMO) at the following landing pages:

879 https://www.bco-dmo.org/dataset/867007; https://www.bco-dmo.org/dataset/867113;

880 https://www.bco-dmo.org/dataset/867221; https://www.bco-dmo.org/dataset/896706

881　**Author contributions.**

882　TT, DV, FK, NL, and JT designed the project. DJY, SK, JT, DR, and TT processed sediment

883　cores at sea. DJY conducted geochemical analyses of sediment porewater and benthic flux

884　chamber water. DJY prepared TOC and TON samples. DR and SK analyzed sediment porosity

885　and density. TT and SK performed shipboard sulfate reduction incubations. DJY and DR

886　conducted sulfate reduction analyses. DJY, NL, and JT transformed and interpreted ROV Jason

887　data. FJ and FW operated BFC and microprofilers and analyzed associated data. XP conducted

888　^{15}N experiments and analyses. All authors reviewed and edited the manuscript.

889

890　**Competing interests.**

891　At least one of the (co-)authors is a member of the editorial board of Biogeosciences.

References

Algar, C. K. and Vallino, J. J.: Predicting microbial nitrate reduction pathways in coastal sediments, Aquatic Microbial Ecology, 71, 223-238, 2014.

An, S. and Gardner, W. S.: Dissimilatory nitrate reduction to ammonium (DNRA) as a nitrogen link, versus denitrification as a sink in a shallow estuary (Laguna Madre/Baffin Bay, Texas), Marine Ecology Progress Series, 237, 41-50, 2002.

Bernhard, J. M., Visscher, P. T., and Bowser, S. S.: Submillimeter life positions of bacteria, protists, and metazoans in laminated sediments of the Santa Barbara Basin, Limnology and Oceanography, 48, 813-828, 2003.

Bograd, S. J., Schwing, F. B., Castro, C. G., and Timothy, D. A.: Bottom water renewal in the Santa Barbara Basin, Journal of Geophysical Research: Oceans, 107, 9-1-9-9, 2002.

Bonaglia, S., Nascimento, F. A., Bartoli, M., Klawonn, I., and Brüchert, V.: Meiofauna increases bacterial denitrification in marine sediments, Nature communications, 5, 5133, 2014.

Boudreau, B. P. and Jorgensen, B. B.: The benthic boundary layer: Transport processes and biogeochemistry, 2001.

Bourbonnais, A., Letscher, R. T., Bange, H. W., Echevin, V., Larkum, J., Mohn, J., Yoshida, N., and Altabet, M. A.: N2O production and consumption from stable isotopic and concentration data in the Peruvian coastal upwelling system, Global Biogeochemical Cycles, 31, 678-698, 2017.

Bremner, J.: Biogenic sediments on the South West African continental margin, 1981.

Brüchert, V., Jørgensen, B. B., Neumann, K., Riechmann, D., Schlösser, M., and Schulz, H.: Regulation of bacterial sulfate reduction and hydrogen sulfide fluxes in the central Namibian coastal upwelling zone, Geochim. Cosmochim. Acta, 67, 4505-4518, 2003.

Caffrey, J. M., Bonaglia, S., and Conley, D. J.: Short exposure to oxygen and sulfide alter nitrification, denitrification, and DNRA activity in seasonally hypoxic estuarine sediments, FEMS microbiology letters, 366, fny288, 2019.

California Cooperative Oceanic Fisheries Investigations: https://www.calcofi.org/ccdata.html, last

Canfield, D. E.: Reactive iron in marine sediments, Geochimica et cosmochimica acta, 53, 619-632, 1989.

Canfield, D. E., Stewart, F. J., Thamdrup, B., De Brabandere, L., Dalsgaard, T., Delong, E. F., Revsbech, N. P., and Ulloa, O.: A cryptic sulfur cycle in oxygen-minimum–zone waters off the Chilean coast, Science, 330, 1375-1378, 2010.

Charoenpong, C. N., Bristow, L. A., and Altabet, M. A.: A continuous flow isotope ratio mass spectrometry method for high precision determination of dissolved gas ratios and isotopic composition, Limnology and Oceanography: Methods, 12, 323-337, 2014.

Cline, J. D.: Spectrophometric determination of hydrogen sulfide in natural waters, Limnol. Oceanogr., 14, 454-458, 1969.

Dale, A. W., Bertics, V. J., Treude, T., and Wallmann, K.: Modeling benthic-pelagic nutrient exchange processes and porewater distributions in a seasonally hypoxic sediment: evidence for massive phosphate release by Beggiatoa?, Biogeosciences, 10, 629-651, 2013.

Dale, A. W., Sommer, S., Lomnitz, U., Bourbonnais, A., and Wallmann, K.: Biological nitrate transport in sediments on the Peruvian margin mitigates benthic sulfide emissions and

936   drives pelagic N loss during stagnation events, Deep Sea Research Part I: Oceanographic
937   Research Papers, 112, 123-136, 2016.

938 Dale, A. W., Sommer, S., Ryabenko, E., Noffke, A., Bohlen, L., Wallmann, K., Stolpovsky, K.,
939   Greinert, J., and Pfannkuche, O.: Benthic nitrogen fluxes and fractionation of nitrate in the
940   Mauritanian oxygen minimum zone (Eastern Tropical North Atlantic), Geochimica et
941   Cosmochimica Acta, 134, 234-256, 2014.

942 Dale, A. W., Sommer, S., Bohlen, L., Treude, T., Bertics, V. J., Bange, H. W., Pfannkuche, O.,
943   Schorp, T., Mattsdotter, M., and Wallmann, K.: Rates and regulation of nitrogen cycling in
944   seasonally hypoxic sediments during winter (Boknis Eck, SW Baltic Sea): Sensitivity to
945   environmental variables, Estuar. Continent. Shelf Sci., 95, 14-28, 2011.

946 Dale, A. W., Sommer, S., Lomnitz, U., Montes, I., Treude, T., Liebetrau, V., Gier, J., Hensen, C.,
947   Dengler, M., Stolpovsky, K., Bryant, L. D., and Wallmann, K.: Organic carbon production,
948   mineralisation and preservation on the Peruvian margin, Biogeosciences, 12, 1537-1559,
949   2015.

950 De Brabandere, L., Bonaglia, S., Kononets, M. Y., Viktorsson, L., Stigebrandt, A., Thamdrup, B.,
951   and Hall, P. O.: Oxygenation of an anoxic fjord basin strongly stimulates benthic
952   denitrification and DNRA, Biogeochemistry, 126, 131-152, 2015.

953 Emery, K., Hülsemann, J., and Rodolfo, K.: Influence of turbidity currents upon basin waters,
954   Limnology and Oceanography, 7, 439-446, 1962.

955 Emmer, E. and Thunell, R. C.: Nitrogen isotope variations in Santa Barbara Basin sediments:
956   Implications for denitrification in the eastern tropical North Pacific during the last 50,000
957   years, Paleoceanography, 15, 377-387, 2000.

958 Fossing, H., Gallardo, V. A., Jørgensen, B. B., Hüttel, M., Nielsen, L. P., Schulz, H., Canfield, D. E.,
959   Forster, S., Glud, R. N., and Gundersen, J. K.: Concentration and transport of nitrate by the
960   mat-forming sulphur bacterium Thioploca, Nature, 374, 713-715, 1995a.

961 Fossing, H., Gallardo, V. A., Jørgensen, B. B., Hüttel, M., Nielsen, L. P., Schulz, H., Canfield, D. E.,
962   Forster, S., Glud, R. N., Gundersen, J. K., Küver, J., Ramsing, N. B., Teske, A., Thamdrup, B.,
963   and Ulloa, O.: Concentration and transport of nitrate by the mat-forming sulphur
964   bacterium Thioploca, Nature, 374, 713-715, 1995b.

965 García-Robledo, E., Corzo, A., and Papaspyrou, S.: A fast and direct spectrophotometric method
966   for the sequential determination of nitrate and nitrite at low concentrations in small
967   volumes, Marine Chemistry, 162, 30-36, 2014.

968 Gier, J., Sommer, S., Löscher, C. R., Dale, A. W., Schmitz, R. A., and Treude, T.: Nitrogen fixation in
969   sediments along a depth transect through the Peruvian oxygen minimum zone,
970   Biogeosciences, 13, 4065–4080, 2016.

971 Glud, R. N., Gundersen, J. K., and Ramsing, N. B.: Electrochemical and optical oxygen
972   microsensors for in situ measurements, in: In situ monitoring of aquatic systems:
973   Chemical analysis and speciation, edited by: Buffle, J., and Horvai, G., Wiley, 2000.

974 Goericke, R., Bograd, S. J., and Grundle, D. S.: Denitrification and flushing of the Santa Barbara
975   Basin bottom waters, Deep Sea Research Part II: Topical Studies in Oceanography, 112,
976   53-60, 2015.

977 Grasshoff, K., Ehrhardt, M., and Kremling, K.: Methods of seawater analysis, Wiley-VCH Verlag
978   GmbH, Weinheim1999.

979   Gundersen, J. K. and Jørgensen, B. B.: Microstructure of diffusive boundary layers and the oxygen
980   uptake of the sea floor, Nature, 345, 604-607, 1990.
981   Hall, P. O. J. and Aller, R. C.: Rapid small-volume flow injection analysis for $\sum CO_2$ and NH_4^+ in
982   marine and fresh waters, Limnol. Oceanogr., 37, 1113-1119, 1992.
983   Hardison, A. K., Algar, C. K., Giblin, A. E., and Rich, J. J.: Influence of organic carbon and nitrate
984   loading on partitioning between dissimilatory nitrate reduction to ammonium (DNRA) and
985   N_2 production, Geochimica et Cosmochimica Acta, 164, 146-160, 2015.
986   Harris, D., Horwáth, W. R., and Van Kessel, C.: Acid fumigation of soils to remove carbonates prior
987   to total organic carbon or carbon‐13 isotopic analysis, Soil Science Society of America
988   Journal, 65, 1853-1856, 2001.
989   Hermans, M., Lenstra, W. K., Hidalgo-Martinez, S., van Helmond, N. A., Witbaard, R., Meysman, F.
990   J., Gonzalez, S., and Slomp, C. P.: Abundance and biogeochemical impact of cable bacteria
991   in Baltic Sea sediments, Environmental science & technology, 53, 7494-7503, 2019.
992   Hossain, M., Bhattacharya, P., Frape, S. K., Jacks, G., Islam, M. M., Rahman, M. M., von Brömssen,
993   M., Hasan, M. A., and Ahmed, K. M.: Sediment color tool for targeting arsenic-safe
994   aquifers for the installation of shallow drinking water tubewells, Science of the Total
995   Environment, 493, 615-625, 2014.
996   Huettel, M., Forster, S., Kloser, S., and Fossing, H.: Vertical migration in the sediment-dwelling
997   sulfur bacteria Thioploca spp. in overcoming diffusion limitations, Applied and
998   Environmental Microbiology, 62, 1863-1872, 1996.
999   Hylén, A., Bonaglia, S., Robertson, E., Marzocchi, U., Kononets, M., and Hall, P. O.: Enhanced
1000   benthic nitrous oxide and ammonium production after natural oxygenation of long‐term
1001   anoxic sediments, Limnology and Oceanography, 67, 419-433, 2022.
1002   Høgslund, S., Revsbech, N. P., Kuenen, J. G., Jørgensen, B. B., Gallardo, V. A., Vossenberg, J. v. d.,
1003   Nielsen, J. L., Holmkvist, L., Arning, E. T., and Nielsen, L. P.: Physiology and behaviour of
1004   marine Thioploca, The ISME journal, 3, 647-657, 2009.
1005   Jensen, M. M., Lam, P., Revsbech, N. P., Nagel, B., Gaye, B., Jetten, M. S., and Kuypers, M. M.:
1006   Intensive nitrogen loss over the Omani Shelf due to anammox coupled with dissimilatory
1007   nitrite reduction to ammonium, The ISME journal, 5, 1660-1670, 2011.
1008   Jeroschewsky, P., Steuckart, C., and Kuehl, M.: An amperometric microsensor for the
1009   determination af H_2S in aquatic environments, Anal. Chem., 68, 4351-4357, 1996.
1010   Jørgensen, B.: Distribution of colorless sulfur bacteria (Beggiatoa spp.) in a coastal marine
1011   sediment, Marine Biology, 41, 19-28, 1977.
1012   Jørgensen, B. B.: A comparison of methods for the quantification of bacterial sulphate reduction
1013   in coastal marine sediments: I. Measurements with radiotracer techniques, Geomicrobiol.
1014   J., 1, 11-27, 1978.
1015   Jørgensen, B. B. and Nelson, D. C.: Sulfide oxidation in marine sediments: Geochemistry meets
1016   microbiology, Geological Society of America, Special Paper 379, 63-81, 2004.
1017   Kallmeyer, J., Ferdelman, T. G., Weber, A., Fossing, H., and Jørgensen, B. B.: A cold chromium
1018   distillation procedure for radiolabeled sulfide applied to sulfate reduction measurements,
1019   Limnol. Oceanogr. Methods, 2, 171-180, 2004.

1020 Kamp, A., de Beer, D., Nitsch, J. L., Lavik, G., and Stief, P.: Diatoms respire nitrate to survive dark
1021   and anoxic conditions, Proceedings of the National Academy of Sciences, 108, 5649-5654,
1022   2011.
1023 Kessler, A. J., Wawryk, M., Marzocchi, U., Roberts, K. L., Wong, W. W., Risgaard‑Petersen, N.,
1024   Meysman, F. J., Glud, R. N., and Cook, P. L.: Cable bacteria promote DNRA through iron
1025   sulfide dissolution, Limnology and Oceanography, 64, 1228-1238, 2019.
1026 Kjeldsen, K. U., Schreiber, L., Thorup, C. A., Boesen, T., Bjerg, J. T., Yang, T., Dueholm, M. S.,
1027   Larsen, S., Risgaard-Petersen, N., and Nierychlo, M.: On the evolution and physiology of
1028   cable bacteria, Proceedings of the National Academy of Sciences, 116, 19116-19125,
1029   2019.
1030 Kononets, M., Tengberg, A., Nilsson, M., Ekeroth, N., Hylén, A., Robertson, E. K., Van De Velde, S.,
1031   Bonaglia, S., Rütting, T., and Blomqvist, S.: In situ incubations with the Gothenburg
1032   benthic chamber landers: Applications and quality control, Journal of Marine Systems,
1033   214, 103475, 2021.
1034 Kraft, B., Tegetmeyer, H. E., Sharma, R., Klotz, M. G., Ferdelman, T. G., Hettich, R. L., Geelhoed, J.
1035   S., and Strous, M.: The environmental controls that govern the end product of bacterial
1036   nitrate respiration, Science, 345, 676-679, 2014.
1037 Kuwabara, J. S., van Geen, A., McCorkle, D. C., and Bernhard, J. M.: Dissolved sulfide distributions
1038   in the water column and sediment pore waters of the Santa Barbara Basin, Geochimica et
1039   Cosmochimica Acta, 63, 2199-2209, 1999.
1040 Levin, L. A., Gutierrez, D., Rathburn, A. E., Neira, C., Sellanes, J., Munoz, P., Gallardo, V. A., and
1041   Salamance, M.: Bethic processes on the Peru margin: a transect across the oxygen
1042   minimum zone during the 1997-98 El Nino, Prog. Oceanog., 53, 1-27, 2002.
1043 Marchant, H. K., Lavik, G., Holtappels, M., and Kuypers, M. M.: The fate of nitrate in intertidal
1044   permeable sediments, PloS one, 9, e104517, 2014.
1045 Marzocchi, U., Bonaglia, S., van de Velde, S., Hall, P. O., Schramm, A., Risgaard‑Petersen, N., and
1046   Meysman, F. J.: Transient bottom water oxygenation creates a niche for cable bacteria in
1047   long‑term anoxic sediments of the Eastern Gotland Basin, Environmental microbiology,
1048   20, 3031-3041, 2018.
1049 Marzocchi, U., Trojan, D., Larsen, S., Louise Meyer, R., Peter Revsbech, N., Schramm, A., Peter
1050   Nielsen, L., and Risgaard-Petersen, N.: Electric coupling between distant nitrate reduction
1051   and sulfide oxidation in marine sediment, The ISME journal, 8, 1682-1690, 2014.
1052 Middelburg, J. and Levin, L.: Coastal hypoxia and sediment biogeochemistry, Biogeosciences, 6,
1053   1273-1293, 2009.
1054 Mortimer, C. H.: The exchange of dissolved substances between mud and water in lakes, Journal
1055   of ecology, 29, 280-329, 1941.
1056 Mosch, T., Sommer, S., Dengler, M., Noffke, A., Bohlen, L., Pfannkuche, O., Liebetrau, V., and
1057   Wallmann, K.: Factors influencing the distribution of epibenthic megafauna across the
1058   Peruvian oxygen minimum zone, Deep Sea Research Part I: Oceanographic Research
1059   Papers, 68, 123-135, 2012.
1060 Mußmann, M., Schulz, H. N., Strotmann, B., Kjær, T., Nielsen, L. P., Rosselló‑Mora, R. A., Amann,
1061   R. I., and Jørgensen, B. B.: Phylogeny and distribution of nitrate‑storing Beggiatoa spp. in
1062   coastal marine sediments, Environmental Microbiology, 5, 523-533, 2003.

Myhre, S. E., Pak, D., Borreggine, M., Kennett, J. P., Nicholson, C., Hill, T. M., and Deutsch, C.: Oxygen minimum zone biotic baseline transects for paleoceanographic reconstructions in Santa Barbara Basin, CA, Deep Sea Research Part II: Topical Studies in Oceanography, 150, 118-131, 2018.

Naik, R., Naqvi, S., and Araujo, J.: Anaerobic carbon mineralisation through sulphate reduction in the inner shelf sediments of eastern Arabian Sea, Estuaries and Coasts, 40, 134-144, 2017.

Noffke, A., Sommer, S., Dale, A., Hall, P., and Pfannkuche, O.: Benthic nutrient fluxes in the Eastern Gotland Basin (Baltic Sea) with particular focus on microbial mat ecosystems, Journal of Marine Systems, 158, 1-12, 2016.

Noffke, A., Hensen, C., Sommer, S., Scholz, F., Bohlen, L., Mosch, T., Graco, M., and Wallmann, K.: Benthic iron and phosphorus fluxes across the Peruvian oxygen minimum zone, Limnol. Oceanogr., 57, 851-867, 2012.

Pavlova, G. Y., Tishchenko, P. Y., Volkova, T., Dickson, A., and Wallmann, K.: Intercalibration of Bruevich's method to determine the total alkalinity in seawater, Oceanology, 48, 438-443, 2008.

Peng, X., Ji, Q., Angell, J. H., Kearns, P. J., Yang, H. J., Bowen, J. L., and Ward, B. B.: Long‐term fertilization alters the relative importance of nitrate reduction pathways in salt marsh sediments, Journal of Geophysical Research: Biogeosciences, 121, 2082-2095, 2016.

Peng, X., Yousavich, D. J., Bourbonnais, A., Wenzhoefer, F., Janssen, F., Treude, T., and Valentine, D. L.: The fate of fixed nitrogen in Santa Barbara Basin sediments during seasonal anoxia, EGUsphere, 2023, 1-26, 2023.

Pfeffer, C., Larsen, S., Song, J., Dong, M., Besenbacher, F., Meyer, R. L., Kjeldsen, K. U., Schreiber, L., Gorby, Y. A., and El-Naggar, M. Y.: Filamentous bacteria transport electrons over centimetre distances, Nature, 491, 218-221, 2012.

Plass, A., Schlosser, C., Sommer, S., Dale, A. W., Achterberg, E. P., and Scholz, F.: The control of hydrogen sulfide on benthic iron and cadmium fluxes in the oxygen minimum zone off Peru, Biogeosciences, 17, 3685-3704, 2020.

Porubsky, W., Weston, N., and Joye, S.: Benthic metabolism and the fate of dissolved inorganic nitrogen in intertidal sediments, Estuarine, Coastal and Shelf Science, 83, 392-402, 2009.

Preisler, A., De Beer, D., Lichtschlag, A., Lavik, G., Boetius, A., and Jørgensen, B. B.: Biological and chemical sulfide oxidation in a Beggiatoa inhabited marine sediment, ISME Journal, 341-351, 2007.

Prokopenko, M., Hammond, D., Berelson, W., Bernhard, J., Stott, L., and Douglas, R.: Nitrogen cycling in the sediments of Santa Barbara basin and Eastern Subtropical North Pacific: Nitrogen isotopes, diagenesis and possible chemosymbiosis between two lithotrophs (Thioploca and Anammox)—"riding on a glider", Earth and Planetary Science Letters, 242, 186-204, 2006.

Qin, Q., Kinnaman, F. S., Gosselin, K. M., Liu, N., Treude, T., and Valentine, D. L.: Seasonality of Water Column Methane Oxidation and Deoxygenation in a Dynamic Marine Environment, Geochimica et Cosmochimica Acta, 2022.

Raiswell, R. and Canfield, D. E.: The iron biogeochemical cycle past and present, Geochemical perspectives, 1, 1-2, 2012.

1105 Reimers, C. E., Ruttenberg, K. C., Canfield, D. E., Christiansen, M. B., and Martin, J. B.: Porewater
1106   pH and authigenic phases formed in the uppermost sediments of Santa Barbara Basin,
1107   Geochim. Cosmochim. Acta, 60, 4037-4057, 1996a.
1108 Reimers, C. E., Ruttenberg, K. C., Canfield, D. E., Christiansen, M. B., and Martin, J. B.: Porewater
1109   pH and authigenic phases formed in the uppermost sediments of the Santa Barbara Basin,
1110   Geochimica et Cosmochimica Acta, 60, 4037-4057, 1996b.
1111 Revsbech, N. P. and Jørgensen, B. B.: Microelectrodes: their use in microbial ecology, in: Adv.
1112   Microb. Ecol., edited by: Marshall, K. C., Plenum, New York, 293-352, 1986.
1113 Robinson, D. M., Pham, A. L., Yousavich, D. J., Janssen, F., Wenzhöfer, F., Arrington, E. C.,
1114   Gosselin, K. M., Sandoval-Belmar, M., Mar, M., and Valentine, D. L.: Iron "Ore" Nothing:
1115   Benthic iron fluxes from the oxygen-deficient Santa Barbara Basin enhance phytoplankton
1116   productivity in surface waters, Biogeosciences Discussions, 1-36, 2022.
1117 Sayama, M.: Presence of nitrate-accumulating sulfur bacteria and their influence on nitrogen
1118   cycling in a shallow coastal marine sediment, Applied and Environmental Microbiology,
1119   67, 3481-3487, 2001.
1120 Schauer, R., Risgaard-Petersen, N., Kjeldsen, K. U., Tataru Bjerg, J. J., B Jørgensen, B., Schramm,
1121   A., and Nielsen, L. P.: Succession of cable bacteria and electric currents in marine
1122   sediment, The ISME journal, 8, 1314-1322, 2014.
1123 Schroller-Lomnitz, U., Hensen, C., Dale, A. W., Scholz, F., Clemens, D., Sommer, S., Noffke, A., and
1124   Wallmann, K.: Dissolved benthic phosphate, iron and carbon fluxes in the Mauritanian
1125   upwelling system and implications for ongoing deoxygenation, Deep Sea Research Part I:
1126   Oceanographic Research Papers, 143, 70-84, 2019.
1127 Schulz, H. N. and Schulz, H. D.: Large sulfur bacteria and the formation of phosphorite, Science,
1128   307, 416-418, 2005.
1129 Schulz, H. N., Jorgensen, B. B., Fossing, H. A., and Ramsing, N. B.: Community structure of
1130   filamentous, sheath-building sulfur bacteria, Thioploca spp., off the coast of Chile, Applied
1131   and Environmental Microbiology, 62, 1855-1862, 1996.
1132 Schulz, H. N., Brinkhoff, T., Ferdelman, T. G., Hernández Mariné, M., Teske, A., and Jørgensen, B.
1133   B.: Dense populations of a giant sulfur bacterium in Namibian shelf sediments, Science,
1134   284, 493-495, 1999.
1135 Seitaj, D., Schauer, R., Sulu-Gambari, F., Hidalgo-Martinez, S., Malkin, S. Y., Burdorf, L. D., Slomp,
1136   C. P., and Meysman, F. J.: Cable bacteria generate a firewall against euxinia in seasonally
1137   hypoxic basins, Proceedings of the National Academy of Sciences, 112, 13278-13283,
1138   2015.
1139 Sholkovitz, E.: Interstitial water chemistry of the Santa Barbara Basin sediments, Geochimica et
1140   Cosmochimica Acta, 37, 2043-2073, 1973.
1141 Sholkovitz, E. R. and Gieskes, J. M.: A PHYSICAL–CHEMICAL STUDY OF THE FLUSHING OF THE
1142   SANTA BARBARA BASIN 1, Limnology and Oceanography, 16, 479-489, 1971.
1143 Sigman, D. M., Robinson, R., Knapp, A., Van Geen, A., McCorkle, D., Brandes, J., and Thunell, R.:
1144   Distinguishing between water column and sedimentary denitrification in the Santa
1145   Barbara Basin using the stable isotopes of nitrate, Geochemistry, Geophysics,
1146   Geosystems, 4, 2003.

Sommer, S., Gier, J., Treude, T., Lomnitz, U., Dengler, M., Cardich, J., and Dale, A. W.: Depletion of oxygen, nitrate and nitrite in the Peruvian oxygen minimum zone cause an imbalance of benthic nitrogen fluxes, Deep-Sea Res. I, 112, 113–122, 2016.

Stramma, L., Johnson, G. C., Sprintall, J., and Mohrholz, V.: Expanding oxygen-minimum zones in the tropical oceans, Science, 320, 655-658, 2008.

Sverdrup, H. and Allen, W.: Distribution of diatoms in relation to the character of water masses and currents off Southern California in 1938, J. mar. Res, 2, 131-144, 1939.

Thunell, R. C.: Particle fluxes in a coastal upwelling zone: sediment trap results from Santa Barbara Basin, California, Deep Sea Research Part II: Topical Studies in Oceanography, 45, 1863-1884, 1998.

Tiedje, J. M., Sexstone, A. J., Myrold, D. D., and Robinson, J. A.: Denitrification: ecological niches, competition and survival, Antonie van Leeuwenhoek, 48, 569-583, 1983.

Treude, T.: Biogeochemical reactions in marine sediments underlying anoxic water bodies, in: Anoxia: Paleontological Strategies and Evidence for Eukaryote Survival, edited by: Altenbach, A., Bernhard, J., and Seckbach, J., Cellular Origins, Life in Extreme Habitats and Astrobiology (COLE) Book Series, Springer, Dordrecht, 18-38, 2011.

Treude, T., Hamdan, L. J., Lemieux, S., Dale, A. W., and Sommer, S.: Rapid sulfur cycling in sediments from the Peruvian oxygen minimum zone featuring simultaneous sulfate reduction and sulfide oxidation, Limnology and Oceanography, 66, 2661-2671, 2021.

Treude, T., Smith, C. R., Wenzhoefer, F., Carney, E., Bernardino, A. F., Hannides, A. K., Krueger, M., and Boetius, A.: Biogeochemistry of a deep-sea whale fall: sulfate reduction, sulfide efflux and methanogenesis, Mar. Ecol. Prog. Ser., 382, 1-21, 2009.

Valentine, D. L., Fisher, G. B., Pizarro, O., Kaiser, C. L., Yoerger, D., Breier, J. A., and Tarn, J.: Autonomous marine robotic technology reveals an expansive benthic bacterial community relevant to regional nitrogen biogeochemistry, Environmental science & technology, 50, 11057-11065, 2016.

Van Cappellen, P. and Ingall, E. D.: Benthic phosphorus regeneration, net primary production, and ocean anoxia: A model of the coupled marine biogeochemical cycles of carbon and phosphorus, Paleoceanography, 9, 677-692, 1994.

Van De Velde, S., Lesven, L., Burdorf, L. D., Hidalgo-Martinez, S., Geelhoed, J. S., Van Rijswijk, P., Gao, Y., and Meysman, F. J.: The impact of electrogenic sulfur oxidation on the biogeochemistry of coastal sediments: A field study, Geochimica et Cosmochimica Acta, 194, 211-232, 2016.

van de Velde, S. J., Hylén, A., Eriksson, M., James, R. K., Kononets, M. Y., Robertson, E. K., and Hall, P. O.: Exceptionally high respiration rates in the reactive surface layer of sediments underlying oxygen-deficient bottom waters, Proceedings of the Royal Society A, 479, 20230189, 2023.

van de Velde, S. J., Hylén, A., Kononets, M., Marzocchi, U., Leermakers, M., Choumiline, K., Hall, P. O., and Meysman, F. J.: Elevated sedimentary removal of Fe, Mn, and trace elements following a transient oxygenation event in the Eastern Gotland Basin, central Baltic Sea, Geochimica et Cosmochimica Acta, 271, 16-32, 2020.

Wallmann, K., José, Y. S., Hopwood, M. J., Somes, C. J., Dale, A. W., Scholz, F., Achterberg, E. P., and Oschlies, A.: Biogeochemical feedbacks may amplify ongoing and future ocean

1190   deoxygenation: a case study from the Peruvian oxygen minimum zone, Biogeochemistry,
1191   159, 45-67, 2022.
1192 Ward, B., Devol, A., Rich, J., Chang, B., Bulow, S., Naik, H., Pratihary, A., and Jayakumar, A.:
1193   Denitrification as the dominant nitrogen loss process in the Arabian Sea, Nature, 461, 78-
1194   81, 2009.
1195 Xuefeng Peng, D. J., Yousavich, A. B., Frank Wenzhoefer,, Felix Jan b en , T., and Valentine, T. a.
1196   D. L.: The fate of fixed nitrogen in Santa Barbara Basin sediments
1197 during seasonal anoxia, 2023.
1198 Zhang, L., Altabet, M. A., Wu, T., and Hadas, O.: Sensitive measurement of NH4+ 15N/14N
1199   (δ15NH4+) at natural abundance levels in fresh and saltwaters, Analytical Chemistry, 79,
1200   5297-5303, 2007.
1201 Zopfi, J., Kjær, T., Nielsen, L. P., and Jørgensen, B. B.: Ecology of Thioploca spp.: nitrate and sulfur
1202   storage in relation to chemical microgradients and influence of Thioploca spp. on the
1203   sedimentary nitrogen cycle, Applied and Environmental Microbiology, 67, 5530-5537,
1204   2001.
1205
1206